DEPARTMENT OF MOLECULAR MEDICINE AND SURGERY
Karolinska Institutet, Stockholm, Sweden

PULMONARY HYPERTENSION AND HEART FAILURE – PHYSIOLOGICAL MARKERS ASSESSED BY CARDIOVASCULAR MAGNETIC RESONANCE

João Ramos

Karolinska Institutet

Stockholm 2020

PULMONARY HYPERTENSION AND HEART FAILURE – PHYSIOLOGICAL MARKERS ASSESSED BY CARDIOVASCULAR MAGNETIC RESONANCE

THESIS FOR DOCTORAL DEGREE (Ph.D.)

By

João Ramos MD

Principal Supervisor:
Martin Ugander MD PhD
Karolinska Institutet
Department of Molecular Medicine and Surgery
Division of Clinical Physiology

Co-supervisor(s):
Björn Wieslander MD PhD
Karolinska Institutet
Department of Molecular Medicine and Surgery
Division of Clinical Physiology

Andreas Sigfridsson PhD
Karolinska Institutet
Department of Molecular Medicine and Surgery
Division of Clinical Physiology

Opponent:
Victor Ferrari MD
University of Pennsylvania
Department of Medicine and Radiology
Perelman Center for Advanced Medicine

Examination Board:
Erik Hedström MD PhD
Lunds Universitet
Department of Clinical Sciences
Unit of Clinical Physiology and Diagnostic
Radiology

Ulrik Sartipy MD PhD
Karolinska Institutet
Department of Molecular Medicine and Surgery

Aristomenis Manouras MD PhD
Karolinska Institutet
Department of Medicine

‘Then loudly cried the bold Sir Bedivere:
“Ah! my Lord Arthur, whither shall I go? […]
now the whole Round Table is dissolved
Which was an image of the mighty world; […]”

And slowly answer'd Arthur from the barge:
“The old order changeth, yielding place to new,
And God fulfils Himself in many ways,
Lest one good custom should corrupt the world.
Comfort thyself: what comfort is in me?”’

Morte d'Arthur, in *Idylls of the King*, Lord Alfred Tennyson

“For serving thee an arm to Arms addrest;
for singing thee a soul the Muses raise;
nought lacks me save of thee to stand confest,
whose duty 'tis the Good to prize and praise:
If Heav'en concede me this, and if thy breast
deign incept worthy of a Poet's lays;
as doth presage my spirit vaticine
viewing thee pace the human path divine […]”

Chant X, *The Lusiads*, Luís Vaz de Camões
(translated by Richard F. Burton)

ABSTRACT

Pulmonary hypertension (PH) is clinically and physiologically associated with heart failure, both with reduced and preserved ejection fraction (HFrEF and HFpEF). In HFpEF, the most likely underlying pathophysiological mechanism is an impairment of left ventricular relaxation named diastolic dysfunction. The close relationship between PH, diastolic dysfunction, and heart failure makes it difficult to clearly distinguish between them in clinical practice. Given the challenges around screening and diagnosis of both PH and diastolic dysfunction, better diagnostic tools are needed to complement the existing ones.

Cardiovascular magnetic resonance (CMR) is considered the most accurate imaging modality in the assessment of myocardial anatomy and function. Furthermore, CMR offers the possibility of qualitatively and quantitatively assess blood flow in large and medium vessels. Constant technical innovations push to further develop the current clinical capabilities of CMR and enable better and faster diagnosis of cardiovascular diseases.

In this thesis, we aimed to expand the current clinical capabilities of CMR in the diagnosis of pulmonary hypertension and diastolic dysfunction, which are not routinely assessed with this imaging modality.

In Study I, we investigated the effect of body position in pulmonary blood flow distribution and documented a new variable, termed pulmonary vascular distensibility reserve, possibly related to left atrial pressure. In Study II, we found that CMR has a higher diagnostic yield than echocardiography for estimation of elevated pulmonary artery pressure. In Study III, CMR estimation of pulmonary artery pressure showed very good agreement with invasively measured pressure, and better sensitivity and accuracy than echocardiography. In Study IV, we developed a high temporal resolution CMR method to measure transmitral blood and myocardial tissue velocities, which had good agreement with echocardiography. Lastly, in Study V, we found that a comprehensive CMR method to diagnose and grade diastolic dysfunction showed very good agreement with echocardiography.

These results suggest that novel and established CMR-based methods can diagnose pulmonary hypertension and diastolic dysfunction. Therefore, CMR may one day play an important role in the diagnostic investigation of these pathologies.

LIST OF SCIENTIFIC PAPERS

I. Wieslander B, **Ramos JG**, Ax M, Petersson J, Ugander M (2019). Supine, prone, right and left gravitational effects on human pulmonary vascular physiology. *J Cardiovasc Magn Reson*. 2019 Nov 11; 21(1):69.

II. **Ramos JG**, Fyrdahl A, Wieslander B, Reiter G, Reiter U, Jin N, Maret E, Eriksson M, Caidahl K, Sörensson P, Sigfridsson A, Ugander M. Cardiovascular magnetic resonance 4D flow analysis has a higher diagnostic yield than Doppler echocardiography for detecting increased pulmonary artery pressure. *BMC Medical Imaging*. 2020 Mar 6; 20(1):28.

III. **Ramos JG**, Wieslander B, Fyrdahl A, Reiter G, Reiter U, Jin N, Skott V, Melin M, Sundblad P, Sigfridsson A, Ugander M. Detecting pulmonary hypertension by cardiovascular magnetic resonance four-dimensional flow analysis or echocardiography – comparison with catheterization. *Manuscript*.

IV. Fyrdahl A, **Ramos JG**, Eriksson MJ, Caidahl K, Ugander M, Sigfridsson A. Sector-wise golden-angle (SWIG) phase contrast with high temporal resolution for evaluation of left ventricular diastolic dysfunction. *Magn Reson Med*. 2020 Apr; 83(4):1310-1321.

V. **Ramos JG**, Fyrdahl A, Wieslander B, Reiter G, Reiter U, Jin N, Maret E, Eriksson M, Caidahl K, Sörensson P, Sigfridsson A, Ugander M. Comprehensive CMR diastolic dysfunction grading shows very good agreement compared to echocardiography. *Manuscript*.

CONTENTS

LIST OF ABBREVIATIONS

2D-PC	Two-dimensional phase contrast
4D	Four-dimensional
CMR	Cardiovascular magnetic resonance
CO	Cardiac output
DD	Diastolic dysfunction
DPG	Diastolic pressure gradient
ECG	Electrocardiography
FFT	Fast Fourier Transform
HFpEF	Heart failure with preserved ejection fraction
HFrEF	Heart failure with reduced ejection fraction
LAVI	Left atrial volume index
LV	Left ventricle
mPAP	Mean pulmonary artery pressure
mPCWP	Mean capillary wedge pressure
PA	Pulmonary artery
PBVV	Pulmonary blood volume variation
PC	Phase-contrast
PH	Pulmonary hypertension
PH-LHD	Pulmonary hypertension due to left heart disease
PVDR	Pulmonary vascular distensibility reserve
PVR	Pulmonary vascular resistance

RHC	Right heart catheterization
RV	Right ventricle
sPAP	Systolic pulmonary artery pressure
SWIG	Sector-wise golden angle
TEE	Transesophagic echocardiography
TPG	Transpulmonary pressure gradient
TR	Tricuspid regurgitant jet velocity
TRPG	Tricuspid regurgitation pressure gradient

1   PULMONARY HYPERTENSION

"The vortex is the point of maximum energy. (…) The vorticist relies on this alone; on the primary pigment of his art, nothing else. (…) All experience rushes into this vortex."

in Vortex (1914), by Ezra Pound

1.1   GENERAL CONSIDERATIONS

Pulmonary hypertension (PH) is defined as a mean pulmonary artery pressure (mPAP) of 20 mmHg or more measured invasively at rest by right heart catheterization (RHC) [1]. PH is etiologically diverse and may be associated with a variety of pre-existing auto-immune, vascular, pulmonary, and/or cardiac conditions.

An mPAP of 12-14 mmHg is considered the average pressure in healthy populations, with an upper normal limit of 20 mmHg. The current mPAP cut-off has been decreased from the previous one of 25 mmHg, i.e. only an mPAP of 25 mmHg or more was considered pathological before the current recommendations; mPAP between 20 and 24 mmHg was referred to by some authors as borderline PH [2].

There are two widely accepted classifications of PH, one based on clinical etiology and the other based on hemodynamic parameters. The clinical classification divides PH into five groups, based on the suspected or confirmed cause of disease. The groups are summarized in Table 1. Hemodynamically, PH may vary in classification based on mainly three invasive parameters: mPAP, mean capillary wedge pressure (mPCWP), and pulmonary vascular resistance (PVR). Table 2 summarizes the hemodynamic classification of PH [2].

PH is uncommon compared to other cardiopulmonary diseases and the epidemiological data is limited; the existing data is mostly based on national population-based cohort studies. In Canada, annual incidence was found to be increasing, with about 28.7 new cases per 100 000 people, with group 2 (PH-LHD) being most common and accounting for a third of total PH cases [3]. In the Netherlands, a population-based study found the prevalence of PH to be 2.6% in the general population, based on echocardiographic data. [4] The burden in healthcare systems is considerable, mostly due to hospitalization costs, and early diagnosis with proper management are essential to reduce costs and improve outcomes [5].

Clinically, PH presents with non-specific symptoms, namely dyspnea, fatigue and possibly syncope and chest pain [6]. Beyond the basic symptoms, the clinical presentation is dependent on the etiology, e.g. dermatological signs in systemic sclerosis and pulmonary signs in lung disease. The pulmonary circulation is in close communication with the right

Table 1 - Clinical classification of pulmonary hypertension (PH)
Group 1 – Pulmonary arterial hypertension (PAH)
Idiopathic, heritable or acquired PAH Persistent PH of the newborn syndrome
Group 2 – Pulmonary hypertension due to left heart disease (PH-LHD)
PH due to HFpEF PH due to HFrEF Valvular heart disease PH secondary to congenital heart disease
Group 3 – Pulmonary hypertension due to lung disease
Obstructive lung disease Restrictive lung disease Mixed obstructive and restrictive lung disease Hypoxia without lung disease Congenital lung disease
Group 4 – Pulmonary hypertension due to pulmonary artery obstruction
Chronic thromboembolic pulmonary hypertension Other obstructions
Group 5 – Pulmonary hypertension with unclear and/or multifactorial mechanisms
Hematological disorders Systemic disorders Others

Adapted from Simmoneau, *et al*. (2019).

Table 2 - Hemodynamic classification of pulmonary hypertension
Pre-capillary pulmonary hypertension
mPAP > 20 mmHg mPCWP ≤ 15 mmHg PVR ≥ 3 WU
Isolated post-capillary pulmonary hypertension
mPAP > 20 mmHg mPCWP > 15 mmHg PVR < 3 WU
Combined pre- and post-capillary pulmonary hypertension
mPAP > 20 mmHg mPCWP > 15 mmHg PVR ≥ 3 WU

mPAP = mean pulmonary artery pressure, PCWP = pulmonary capillary wedge pressure, PVR = pulmonary vascular resistance, WU = Wood units. Adapted from Simmoneau, *et al.* (2019).

heart, and a concomitant presentation of PH and right-sided heart failure is common and carries a higher risk of death.

The diagnosis of PH starts with a clinical suspicion based on presentation, which then motivates a diagnostic workup where non-invasive imaging plays a major role. All patients with suspicion of PH have an indication to perform transthoracic echocardiography (TTE) [7], which can yield a probability of PH, based on Doppler estimation of elevated PA pressure, right ventricle characteristics, and right atrial dimensions. To definitively diagnose PH, however, it is necessary to perform a RHC to comprehensively assess the hemodynamic parameters of the pulmonary circulation [8].

1.2   PATHOPHYSIOLOGY

In vascular physiology, in particular with regards to hypertension, there are two variables crucial to explaining PH, namely, compliance and resistance [9].

Compliance in a vessel of fixed length L is given by the formula:

$$C = \frac{\Delta V}{\Delta P} \tag{1}$$

where C is compliance in ml/mmHg, ΔV is the change in volume in ml and ΔP is the change in pressure in mmHg [9]. Therefore, high compliance in a vessel means that it can passively increase in volume to accommodate an increasing stroke volume while maintaining a relatively low change in pressure.

Vascular resistance in a vessel of fixed length L and radius r is given by:

$$R = \frac{\Delta P}{Q} \tag{2}$$

where R is resistance in mmHg·s/L, ΔP is the change in pressure in mmHg and Q is flow in ml/s [9]. In the pulmonary circulation, the corresponding formula is:

$$PVR = \frac{mPAP - mPCWP}{CO} \tag{3}$$

where PVR is pulmonary vascular resistance in mmHg·min/L (Wood units), mPAP is the mean pulmonary artery pressure in mmHg, mPCWP is the mean pulmonary capillary wedge pressure (equivalent to left atrial pressure) in mmHg, and CO is the cardiac output in L/min [10].

The pulmonary circulation is comprised of the pulmonary arteries and veins, as well as their numerous branches distributed across the lung parenchyma. Compared to the systemic circulation, the most striking feature of the pulmonary circulatory system is that it has a high compliance, low resistance vessel network [11]. Mean compliance and resistance of the pulmonary circulation is 3.8-12 ml/mmHg and 0.11 mmHg.s/ml, respectively, in contrast with the systemic circulation, 0.4-3.8 ml/mmHg and 1.0 mmHg.s/ml, respectively [11] [12] [13]. Furthermore, while 80% of the total compliance in the systemic circulation is attributed to the compliance of the proximal aorta, the opposite is true for the pulmonary circulation, in which the numerous distal branches of the pulmonary arteries account for the lion's share of the arterial compliance [11].

Resistance and compliance share a hyperbolic relationship [14], as shown in Figure 1. The product of resistance and compliance is referred to as RC time, and RC time is a constant in both healthy and PH populations [15]. Taken together, this means that a decrease in compliance eventually leads to an elevated resistance, yet sharp decreases in compliance may occur before any meaningful increases in resistance.

While the variables discussed above pertain to vascular physiology, they have a profound impact on cardiac function as well. Accordingly, the Windkessel model states that right ventricular (RV) afterload is dependent on three variables [13] [16]:

- Resistance, i.e. PVR, accounts for about 75% of total RV afterload and is also described as static afterload, since it represents the opposition to flow (as shown in equation 2).

- Compliance, is highly distributed among the numerous distal branches of the pulmonary arteries and accounts for about 23% of total RV afterload. It represents the pulsatile component of afterload, i.e. the energy required to overcome increased pressures and allow flow in the circuit.

- Impedance, is defined as the effect of the mass of blood on afterload. It is both hard to measure and a very small component of RV afterload, 1-2%, and therefore not routinely analyzed [11].

Lastly, an additional physiological variable of relevance is pulse wave velocity (PWV), which refers to the velocity of a pressure/flow wave that propagates through a vessel as a result of the passage of blood [17]. Abnormal wave propagation has been documented in PH patients, as well as elevation of PWV [18]. The latter is an indicator of decreased compliance, as it represents an impaired ability of the vessel to distend.
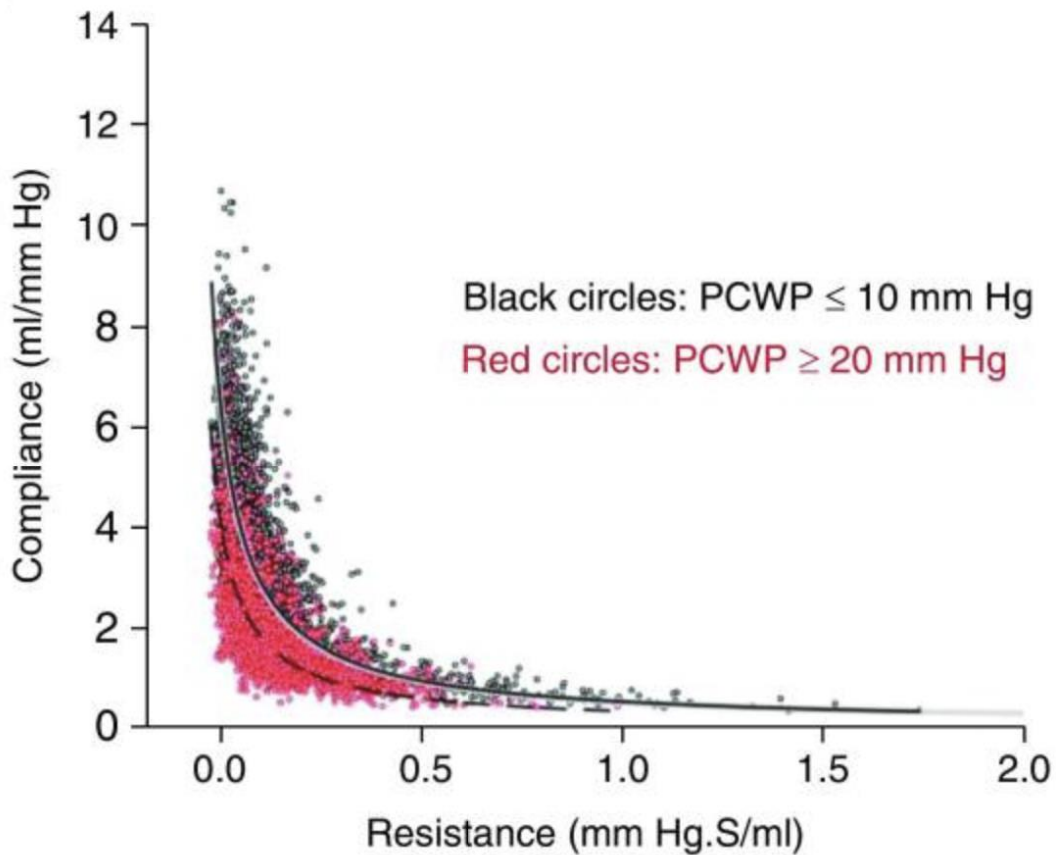
Figure 1 – The inverse hyperbolic relationship between compliance and resistance in pre- and post-capillary hypertension. Black data points represent patients with pre-capillary PH and red data points represent patients with post-capillary PH. Reprinted with permission of the American Thoracic Society, from Thenappan et al. (2015) [14].

Pre-capillary PH is characterized by a decrease in compliance of the pulmonary circuit, and this is one of the physiological hallmarks of the disease (Figure 2) [19] [20]. This is mainly due to an increase in arterial stiffness as a consequence of intima disruption, which leads to further endothelial dysfunction and remodeling [21]. Loss of compliance means an increase in PVR and in right ventricular (RV) afterload, which may in turn lead to RV dysfunction and, ultimately, death.

On the other hand, in post-capillary PH, the defining feature is the elevation of mPCWP, which results from a backward propagation of pressure to the pulmonary vasculature from the left atrium [22]. In this case, for any given PVR, pulmonary vessel compliance is also reduced, leading to the biochemical changes described above. If endothelial remodeling occurs only to a lesser extent, the condition is referred to as *isolated post-capillary PH*. If, however, high levels of vessel remodeling occur, then the condition is referred to as *combined pre- and post-capillary PH*.
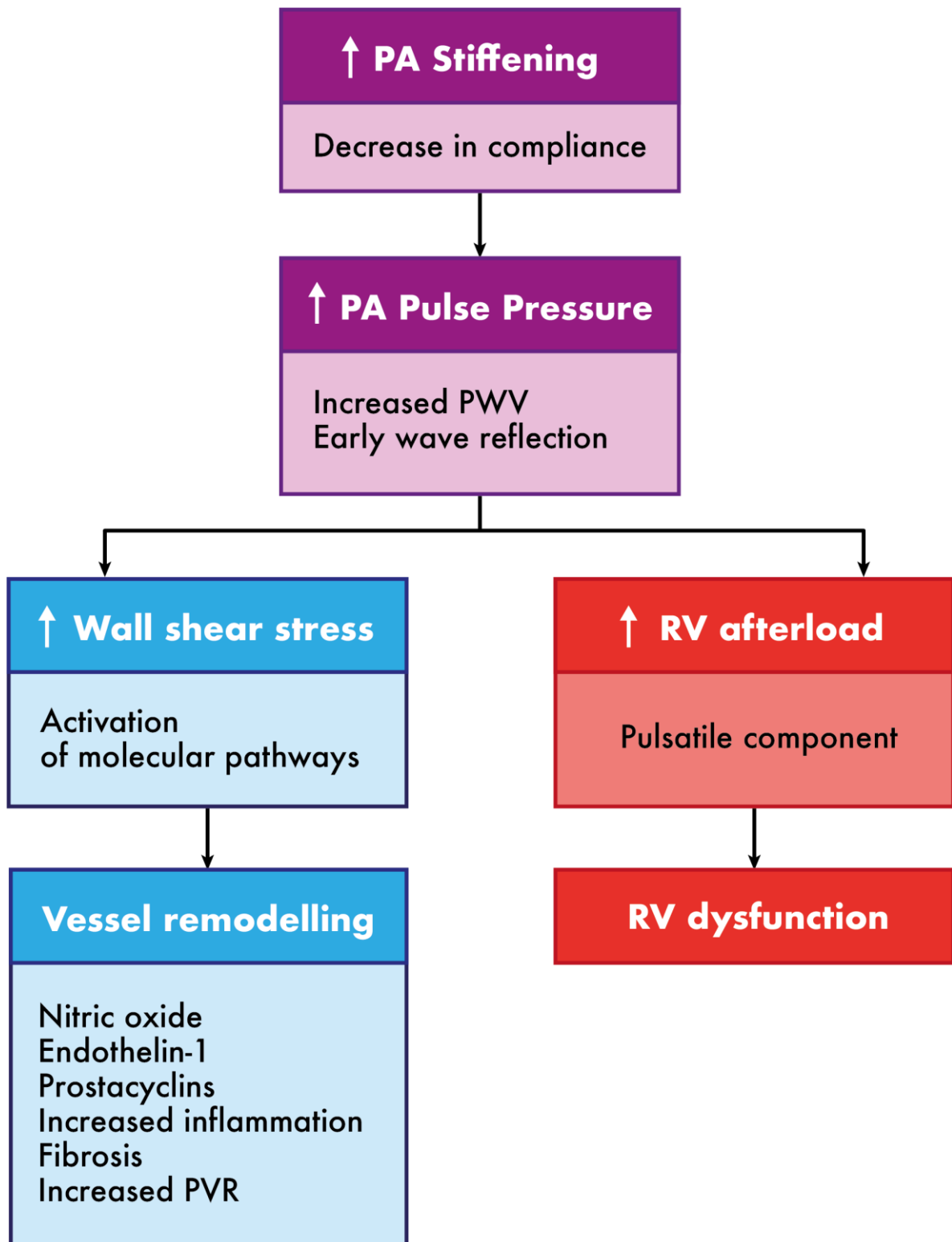
14

Figure 2 – Summary of the pathophysiology of PH. Vessel stiffness and decreased compliance are thought to be the initial changes that trigger endothelial remodeling and cardiac adaptions to the increased workload. PA – pulmonary artery, PWV – pulse wave reflection, RV – right ventricle, PVR – pulmonary vascular resistance.

Vortex formation in the PA, detected by CMR 4D flow analysis, is a pathophysiological phenomenon of diagnostic interest for all types of PH. The presence of vortices in aortic and ventricular flow has been well documented, but its clinical significance is not always clear [23] [24]. In the specific case of the PA, late-systolic to diastolic vortex duration (as a percentage of the cardiac cycle) has been shown to be linearly correlated with mPAP in all PH subtypes [25] [26].

Vortex formation is a complex process best described by fluid dynamics, which is outside the scope of this thesis. In general terms, vortex formation in PH seems to be dependent on two factors; on the one hand, there is an earlier inversion of the PA-RV pressure gradient compared to healthy patients. In contrast, in normal conditions, the PA-RV gradient starts as negative in early systole (RV pressure is greater than PA pressure), becomes approximately 0 in mid-systole (equalization of RV and PA pressures) and then positive in late systole (PA pressure greater than RV pressure) [27]. On the other hand, this pathological development of the pressure gradient over time favors the formation of a luminal boundary layer [28], due to a shift in maximal flow velocity from the center of the vessel to the anterior wall, as shown in Figure 3. Boundary layers are prone to hosting backward flow that then completes the circular formation of a blood flow vortex.

In PH, not only is a vortex observed, but its duration is highly correlated with mPAP. Presumably, vortex formation is a physiological process that preserves some of the kinetic energy associated with blood flow in a vessel with reduced compliance and increased resistance [25]. Under these conditions, forward blood flow to the distal branches of the PA is impaired and kinetic energy is instead partially conserved in the vessel as a vortex.

The exact methodology used to assess the duration of blood flow vortices in PH is described in detail under the Imaging section of this chapter.
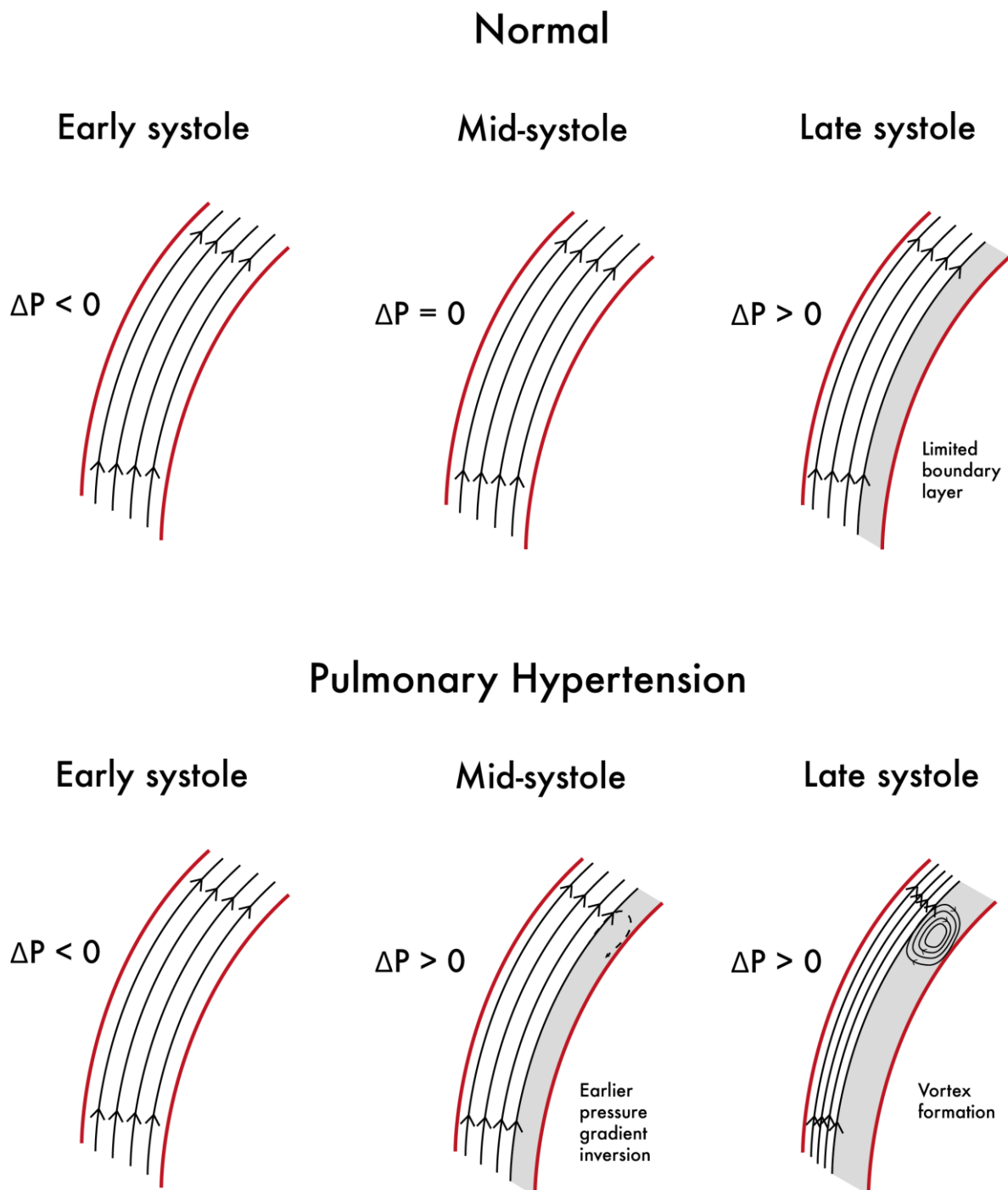
Figure 3 – Representation of PA-RV pressure gradient (ΔP) inversion and vortex formation in both normal individuals and PH patients. The red lines represent the wall of the pulmonary artery. The black arrows represent streamlines of PA blood flow. The gray shaded area represents the boundary layer that allows a vortex to form.

1.2.1 Pulmonary Blood Volume Variation

In Study I, which focused on normal pulmonary physiology, we use a previously described variable referred to as *pulmonary blood volume variation* (PBVV) [29]. PBVV reflects the change in blood volume present in the pulmonary circulation during the cardiac cycle.

To calculate PBVV, five sets of measurements are required: (1) pulmonary artery flow, (2) flow in all four pulmonary veins. With these data, as exemplified on Figure 4, PBVV in mL is calculated from the curve resulting from the cumulative integral of the difference between arterial and venous pulmonary blood flow. PBVV was shown to be reduced after myocardial infarction in a pig model [29]. It was also shown to remain unchanged in systemic sclerosis compared to normal controls [30].
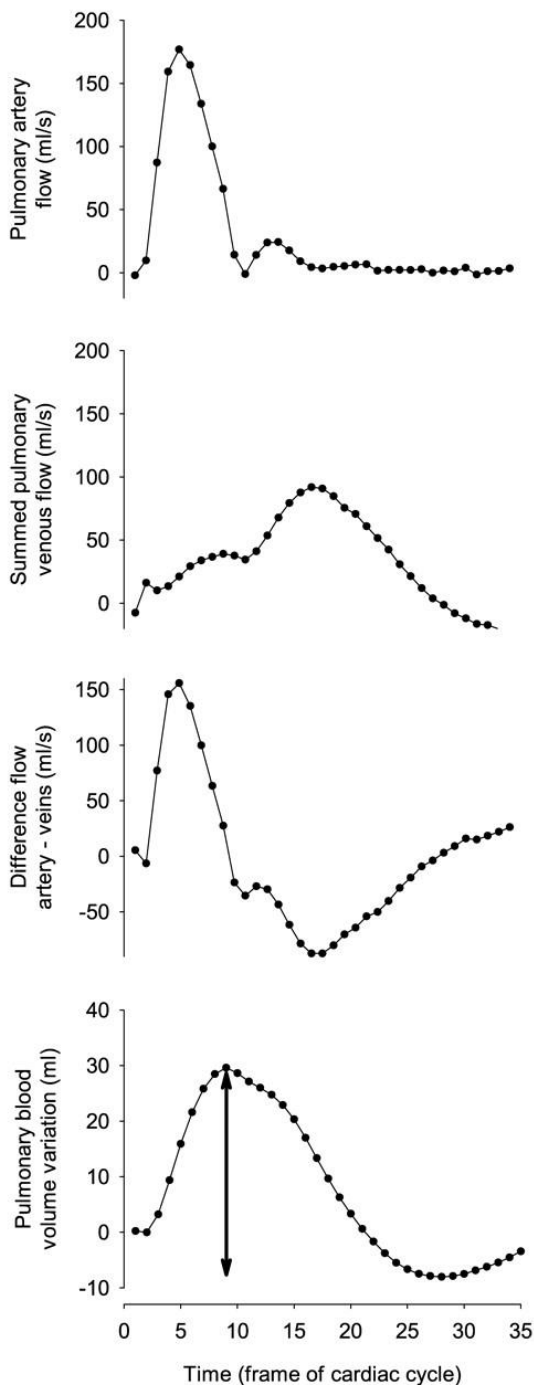

Figure 4 – Charts detailing how PBVV is calculated. From top to bottom, Row 1: Flow in the pulmonary artery during one cardiac cycle. Row 2: Summed flow of all four pulmonary veins during one cardiac cycle. Row 3: Difference between the curves in rows 1 and 2, i.e. the difference between pulmonary arterial and venous flow during one cardiac cycle. Row 4: Cumulative integral of the curve shown in Row 3, PBVV during one cardiac cycle. The arrow represents the difference between the minimum and maximal value of the curve, which corresponds to PBVV in mL. Reprinted with permission from Ugander, *et al.* (2009) [29].

1.3 IMAGING

Imaging plays a central role in screening for PH and is one of the components of a set of tests required to paint a complete picture of the patient with PH [31].

Whenever a patient's clinical presentation is suggestive of PH, echocardiography is indicated to assess the risk of PH given a set of criteria. Based on the result of this assessment, the patient may be referred to RHC, which is required to establish a definitive diagnosis and classify PH hemodynamically. For patients where CTEPH is suspected, a V/Q scan is also performed [32].

1.3.1 Echocardiography

In transthoracic echocardiography (TTE), screening for PH is based on Doppler measurement of the tricuspid regurgitation jet velocity, TR, in m/s [33]. From this value, by applying the Bernoulli equation, one can derive the tricuspid regurgitation pressure gradient (TRPG), in mmHg, as follows:
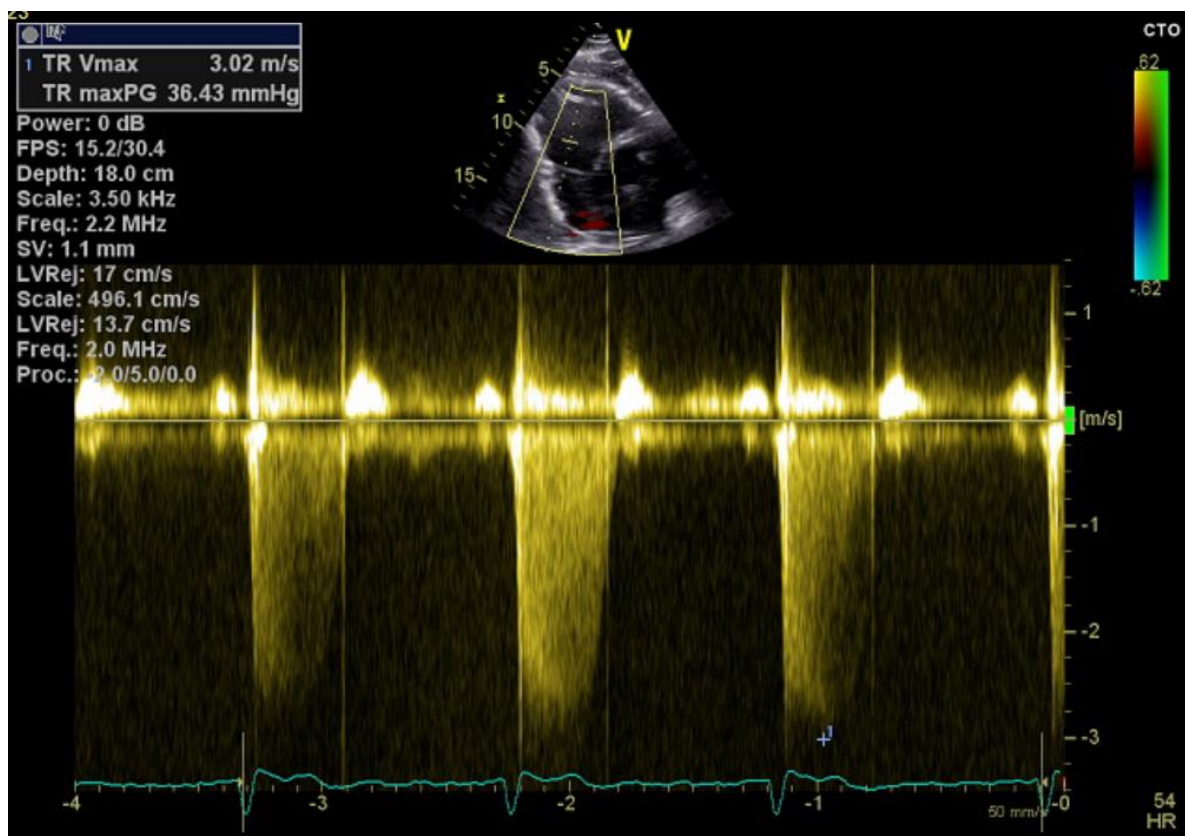
$$TRPG = 4TR^2 \tag{4}$$

Figure 5 – Maximal tricuspid regurgitation velocity measurement by Doppler echocardiography. This patient had a measured TR of 3 m/s which corresponded to a TRPG of 36 mmHg.

Systolic pulmonary artery pressure (sPAP), in mmHg, can then be derived by TRPG, by adding right atrial pressure (RAP) in mmHg:

$$sPAP = TRPG + RAP \tag{5}$$

mPAP can also be estimated with echocardiography, by applying Chemla's empirically derived equation [34], which uses sPAP as follows:

$$mPAP = 0.61 \cdot sPAP + 2 \tag{6}$$

RAP estimation by echocardiography yields poor agreement with invasive measurements, with an accuracy as low as 34% [35]. Therefore, TR or TRPG are instead commonly used to draw conclusions about the probability of PH in a given patient. If a TR is measured as greater than 2.8 m/s, the probability of PH is considered intermediate; if TR is greater than 3.4 m/s, the probability is considered to be high [36]. However, other echocardiographic signs may be considered in this assessment, adding to the probability of PH if they are positive. These signs include RV and RA dimensions, PA flow acceleration time, PA diameter and inferior vena cava diameter [37].

Echocardiography is a useful tool to screen for PH, but is not recommended as the sole tool for diagnosis. While correlation between echocardiographic sPAP and invasive sPAP is good on a group level (Spearman correlation 0.52-0.69) [38][39], echocardiography may considerably over- or underestimate PA pressures compared to RHC in the individual patient [40]. There is also some debate in regards to the TR cut-off used to diagnose PA pressures, and it has been suggested that a lower cut-off of 2.7 m/s, equivalent to TRPG 30 mmHg, would be more adequate to indicate a high probability of PH and a considerable increase in mortality risk [41].

1.3.2 CMR

In the routine assessment of PH, CMR may be of value due to the reliability of its volumetric measurements [42]. Decreased RV volume, RV stroke volume, RV mass or LV preload are indicative of worse prognosis and higher risk of death in PH [43]. T1 mapping techniques have also been used to characterize the RV myocardial tissue, possibly identifying fibrotic changes and correlating well with pulmonary hemodynamics [44]. However, these methods should be interpreted with caution due to the limitations in spatial resolution.

Nevertheless, none of these analyses are directly predictive of hemodynamic variables associated with PH. Recent advances in phase contrast MR (PC-MR) have made possible to evaluate RV and PA flow, with varying degrees of success and accuracy in diagnosing PH. The following methods have been described:

- *PA flow velocity*: measuring the average flow velocity in the main PA (Figure 6) has been described as a possible predictor of mPAP and PVR [45], given that that flow velocity is reduced in PH as a result of vessel changes.

- *PA cross-sectional area change*: in vessels with reduced compliance, i.e. impaired ability to distend, vessel cross-sectional change as a percentage of the difference between maximal and minimal area should be decreased compared to normal. This method shows only moderate agreement with mPAP and PVR [46].

- *Relative onset of retrogade flow (rROF)*: PC-MR allows for the quantification of retrograde flow during the cardiac cycle, if present. One study concluded that in PH patients, there is an earlier onset of retrograde flow compared with healthy individuals [47]. Although capable of diagnosing PH with high accuracy, this method cannot estimate relevant hemodynamic variables (mPAP or others).

- *Multiparametric models*: several models that take into acccout multiple variables (PA flow, RV stroke volume, cross-sectional area change, etc.) have been suggested to predict both PVR and mPAP [48] [49].

- *Vortex analysis*: as shown in Figure 3, vortex formation is related to the pathophysiology of PH and can be assessed by CMR 4D flow analysis, with excellent predictive power compared to invasive mPAP [25] [26].
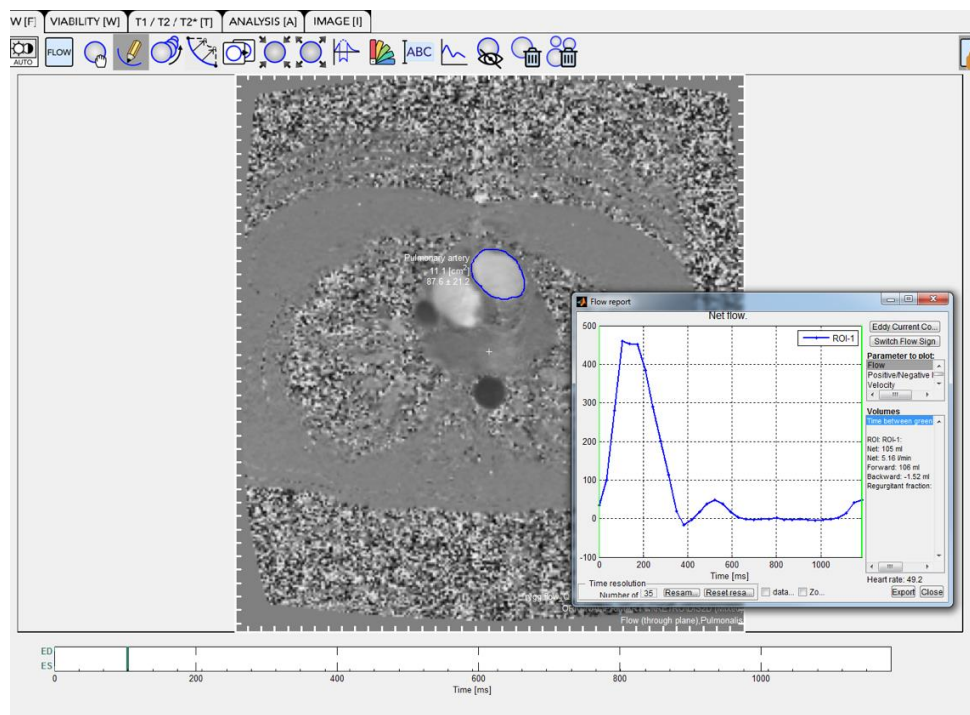

Figure 6 – Measurement of PA flow during the cardiac cycle from a 2D phase contrast image stack in a healthy volunteer with the program Segment (Medviso, Lund, Sweden).

Among all these methods, estimation of mPAP from vortical blood flow duration in the main PA is the method that has shown the best correlation with invasive mPAP. This is the method used in the studies included in this thesis. Both phase contrast MR and 4D flow analysis of vortical blood flow are discussed in more detail in Chapter 3.

2 HEART FAILURE

> "As for you, my galvanized friend, you want a heart. You don't know how lucky you are not to have one. Hearts will never be practical until they are made unbreakable."
>
> *in The Wizard of Oz* (1900), L. Frank Baum

2.1 GENERAL CONSIDERATIONS

Heart failure (HF) is a syndrome characterized by the inability of the heart to perform its main physiological function – pumping blood through vessels to meet the metabolic demands of the body's tissues while retaining normal cardiac filling pressures [9]. Symptoms are usually non-specific and include dyspnea, peripheral edema and varying degrees of fatigue.

HF is frequently associated with one of three major etiological groups, namely arrhythmia, myocardial disease, or abnormal loading. The first group refers to chronic tachy- and bradyarrhythmias that disrupt the heart's ability to maintain its cardiac output. The second group includes common syndromes such as ischemic heart disease (including myocardial scar and microvascular dysfunction), infiltration disease (i.e. amyloidosis, hemochromatosis and Fabry's disease), cardiomyopathies and others. The last group refers to chronically increased preload or afterload, as it is the case of arterial hypertension, valvular disease and fluid overload (for example as a result of kidney failure) [50].

Clinically, HF is usually subdivided into one of three groups, based on the measurement of left ventricular ejection fraction (LVEF):

- Heart failure with reduced ejection fraction (HFrEF), where LVEF is determined to be less than 40%

- Heart failure with preserved ejection fraction (HFpEF), where LVEF is measured as more than 50%

- Heart failure with mid-range ejection fraction (HFmrEF), with a LVEF between 40 and 49%, which is considered as a middle ground between the two previous conditions

This subdivision is clinically relevant inasmuch as etiology, complications and therapeutic decision-making vary across groups. Furthermore, while HFrEF is characterized by systolic dysfunction, HFpEF is most likely predominantly caused by diastolic dysfunction. HFmrEF is thought to share characteristics from both systolic and diastolic dysfunction and its pathophysiology is incompletely understood [51].

2.2 DIASTOLIC DYSFUNCTION

Diastolic dysfunction (DD) is defined as an impairment of LV relaxation and consequent increase in LV filling pressures. Furthermore, DD is the most likely pathophysiological mechanism responsible for HFpEF [51] [52]. In contrast to HFrEF, the diagnosis and grading of HFpEF remains challenging, mostly because of the difficulty in clearly defining diastolic dysfunction and reliably measuring the physiological variables associated with it [53]. Moreover, the current therapeutic alternatives have not shown to reduce mortality in patients with HFpEF [54].

Heart failure has a total prevalence of 2-3% in the general population, with increasing prevalence in older patient cohorts. In the total heart failure population, 44% have preserved EF and 28% have DD. Twenty-one per cent of DD patients are asymptomatic [55].

The physiology underlying DD is complex, involving several biochemical pathways and changes in myocardial characteristics, the pulmonary circulation, and both the atria and ventricles. Hence, there is no clear general definition of diastolic dysfunction in the literature [56] [57]. When diagnosed by echocardiography, DD is usually graded into I-III with higher grades representing higher mortality risk [58].

2.2.1 Pathophysiology

According to the Frank-Starling law (Figure 7), the volume of blood ejected from the heart (stroke volume) depends on the volume of blood present in the ventricle at late diastole (preload, measured as left ventricular end diastolic volume) [9]. During exercise, this means that the healthy heart will accommodate more blood during diastole, and eject more blood during systole. The former is highly dependent on the ventricle's ability to relax, i.e. its relaxation rate. An increased ventricle relaxation rate allows it to fill at low pressures and thus maintain a stroke volume that is adequate for the level of exertion.

Elevated LV filling pressures (LVP) are therefore thought to be one the primary factors affecting diastolic function. Nevertheless, elevated LVP are not synonymous with DD, as cases of DD have been recorded with normal LVP. In contrast, normal diastolic function can be compatible with elevated LVP [59].

Two other LV parameters influence LV filling pressures, namely LV relaxation rate and LV chamber stiffness, which reflect not only aspects of the myocardium at a cellular level, but also LV geometry [60]. LV relaxation rate is sometimes used as the invasive reference method for diagnosing DD and corresponds to the time constant of isovolumetric pressure decay (*tau*, Figure 8).
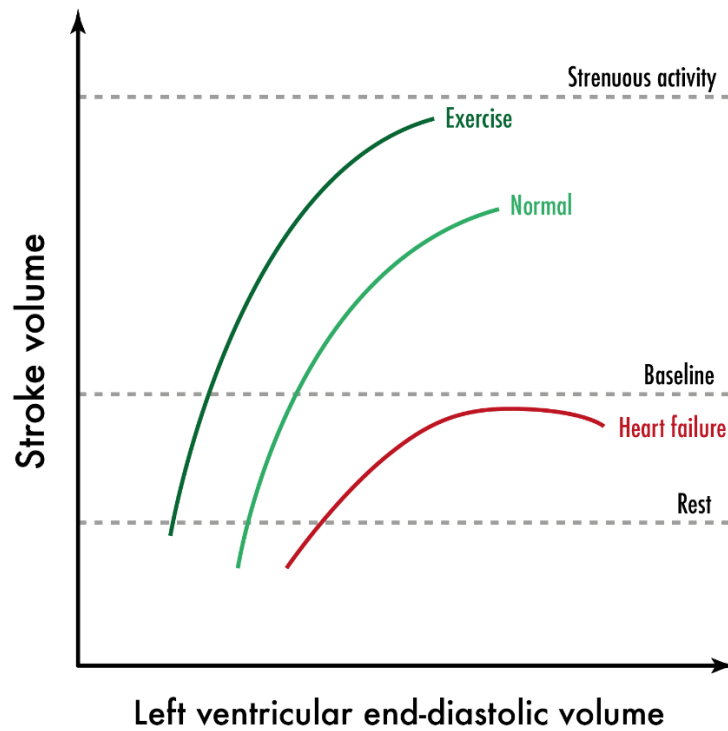
Figure 7 – Graphical representation of the Frank-Starling mechanism. Under normal conditions and physical exercise on a healthy individual, the heart ejects more blood (stroke volume) in response to a higher preload. Under heart failure conditions, its ability to adapt to higher preload is compromised.
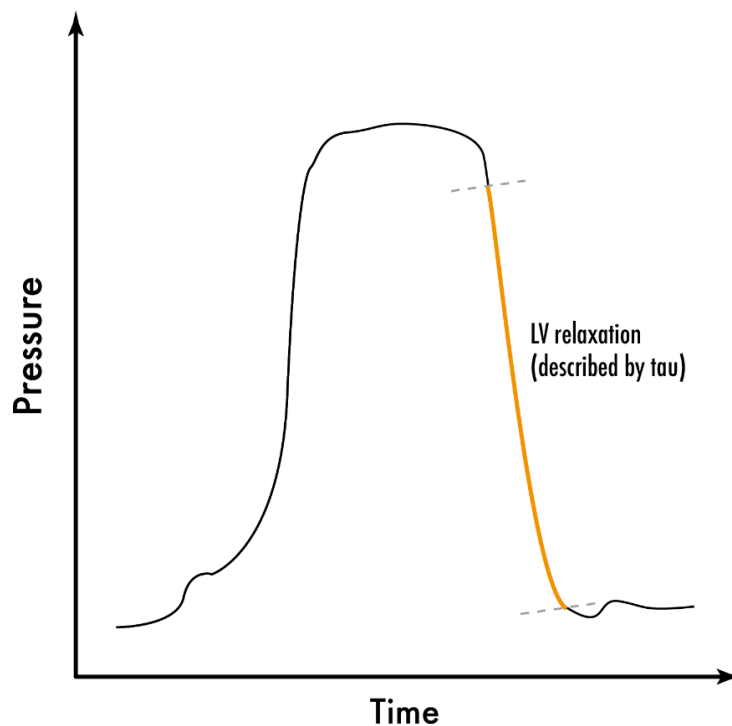

Figure 8 – LV pressure-time curve during one cardiac cycle. After aortic valve closure, the LV relaxes, resulting in a rapid reduction of pressure over time. The slope of the exponential fit of the descending portion of this curve corresponds to tau or LV relaxation rate, which is decreased in DD.
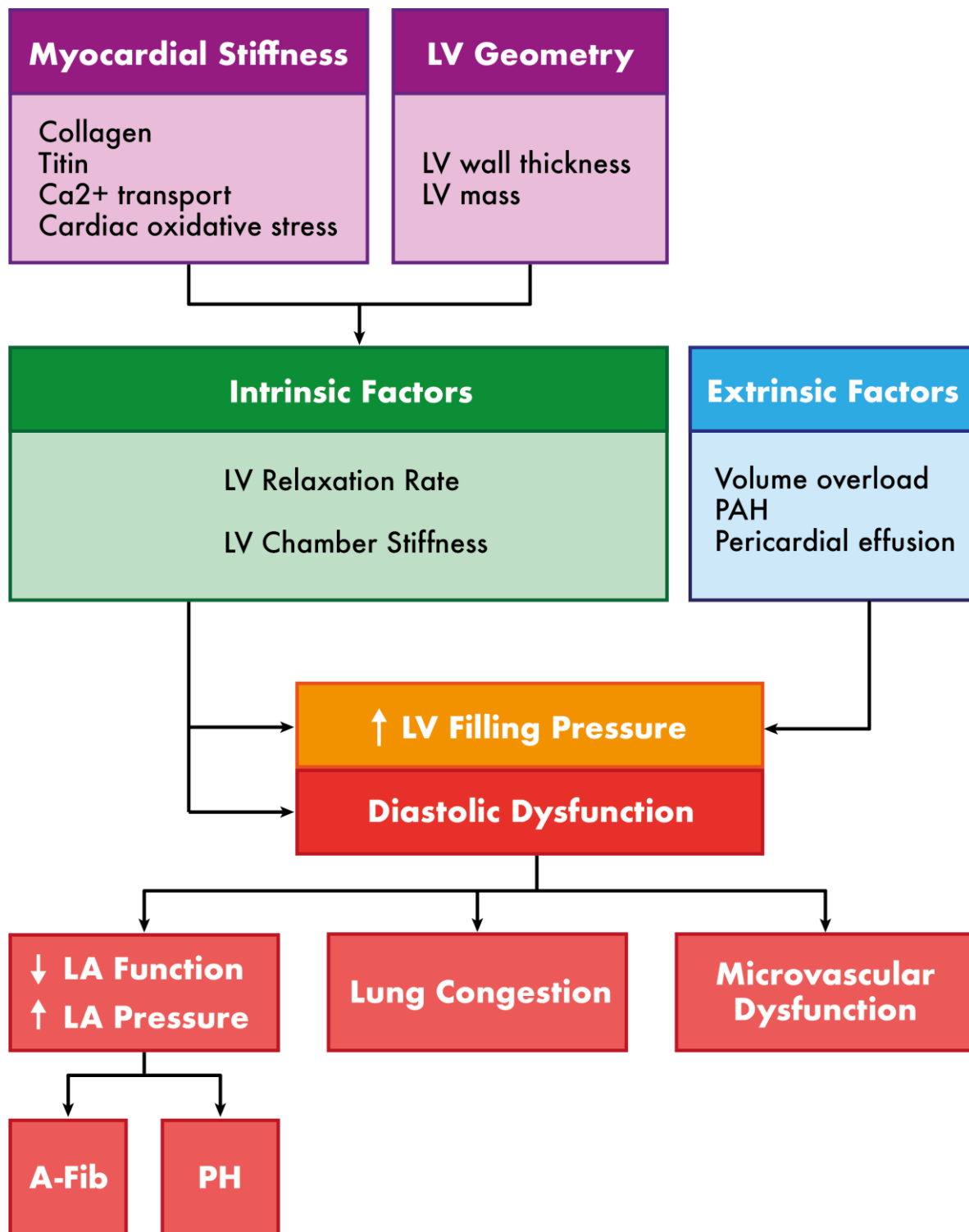
Figure 9 – Summary of the pathophysiology of elevated LV filling pressures and diastolic dysfunction. Factors intrinsic to the LV cause elevated filling pressures and diastolic dysfunction, while external factors (such as volume overload) may elevate LV filling pressures but not necessarily cause diastolic dysfunction. LA dysfunction (with resulting atrial fibrillation and PH), lung congestion and microvascular dysfunction (ultimately myocardial ischemia) are consequences of chronic diastolic dysfunction. LV – left ventricle, PAH – pulmonary arterial hypertension, LA – left atrium, A-Fib – atrial fibrillation, PH – pulmonary hypertension. Adapted from Litwin et al. (2019) [60].

Regarding myocardial abnormalities at a cellular level, several mechanisms have been proposed as potentially responsible for the myocardial stiffness observed in DD. Delayed Ca^{2+} transport and increased diastolic Ca^{2+} concentrations could impair the relaxation of the cardiomyocyte. Changes in handling proteins and cellular receptors involved with Ca^{2+} transport are thought to be a result of the nefarious effect of reactive oxygen species [61]. On the other hand, impaired phosphorlyation of titin, a key molecule in muscle contraction and relaxation, was found in HFpEF molecular models [61]. Fibrosis and changes to collagen degradation pathways are also a contributor to impaired myocardial relaxation [62]. However, none of these changes have been proven to be solely a result of diastolic dysfunction, nor is it yet possible to reliably assess them in the clinical setting [63].

LV geometry also influences its ability to fully relax. Specifically, increased wall thickness and LV mass influence relaxation. If pathologically increased, these two variables may point to the diagnosis of LV concentric hypertrophy, which is typically associated with diastolic dysfunction [64]. Nonetheless, patients with HFpEF may present with a diverse range of cardiac phenotypes, including normal morphology [59]. LV geometry parameters are usually assessed by echocardiography or CMR, as detailed in later sections.

As a consequence of the changes observed in the LV, the left atrium (LA) may undergo remodeling in an attempt to preserve LA function. Increased LA volumes and pressure will eventually be transmitted backwards to the pulmonary circulation, resulting in pulmonary hypertension [22], as described in the previous chapter. Elevated PA pressure is therefore a relevant marker in the assessment of diastolic function and translates into worse clinical outcomes [65] [66]. Both LA dysfunction and pulmonary hypertension may also result in right ventricular hypertrophy, which is another factor that is associated with increased risk of death [52].

2.3   IMAGING

Echocardiography is recommended as the first line imaging modality for diagnosis of HF and is also useful in risk stratification and follow-up [67]. Its main strengths are wide availability, relatively low cost and safety, while operator dependency and limited acoustic windows rank among the main drawbacks. Echocardiography plays an important role in both HFrEF, with measurement of LVEF and characterization of the LV, and HFpEF, with several diastolic variables being measured in order to diagnose and grade DD [68].

Concurrently, CMR plays an increasingly important role in the diagnosis of HF, becoming in recent years the reference standard for measurement of ventricular mass and dimensions [68]. Techniques involving gadolinium-based contrast agents combined with T1 mapping are useful in characterizing the myocardium and determining etiology [69]. Although the role of

CMR in HFrEF is well established, HFpEF represents somewhat of a limitation, since not all diastolic parameters are routinely tested with CMR [70].

Other modalities, such as SPECT, PET and invasive coronary angiography are also an integral part of the diagnostic arsenal in HF, but beyond the scope of this thesis which focuses on echocardiography and CMR.

2.3.1 Echocardiography

Evaluation of diastolic function by echocardiography involves measuring several variables of physiological relevance for diastolic dysfunction, and applying an algorithm (Figure 10) that yields a grade of DD based on those variables. Table 3 lists the main variables measured in clinical routine and which are necessary to have in order to apply these diagnostic algorithms [71]. However, several other variables may be useful to further characterize diastolic function in the individual patient [56].

The main mitral inflow parameters, peak E and A-wave velocities, reflect the diastolic LA-LV pressure gradient, and, therefore, left-sided filling pressures. However, numerous other clinical and physiological factors may influence the interpretation of these parameters, such as age, heart rate, arrhythmia, and LA function. Importantly, advanced age tends to decrease peak E-wave velocity and the E/A ratio, while increasing peak A-wave velocity [72].

The myocardial tissue velocities, lateral, septal, and average e', indicate the early diastolic lengthening velocity of LV muscle fibers. A decreased average e' is an early marker of DD and suggests a poorer prognosis [73]. Furthermore, average e' is correlated with tau and invasively measured LV end-diastolic pressure [74].

Left atrial volume index (LAVI) correlates physiologically with LA function. Since the LA is subject to high filling pressures in the context of DD, this will result in LA remodeling and increase in volume [60]. LA volume is independently correlated with all-cause mortality [75], and also of the severity of DD in the individual patient [76].

Several authors report that these echocardiographic criteria are reliable and show moderate to good agreement with invasive measurements of LV filling pressures and PCWP. Echocardiography showed a sensitivity/specificity of 87%/88% compared to invasive measurements of PCWP in a multicentric study, with an accuracy of 87% [77]. In another study using invasively measured LV end-diastolic pressure as reference, the authors reported a sensitivity/specificity of 75%/74% and accuracy of 75% [78].
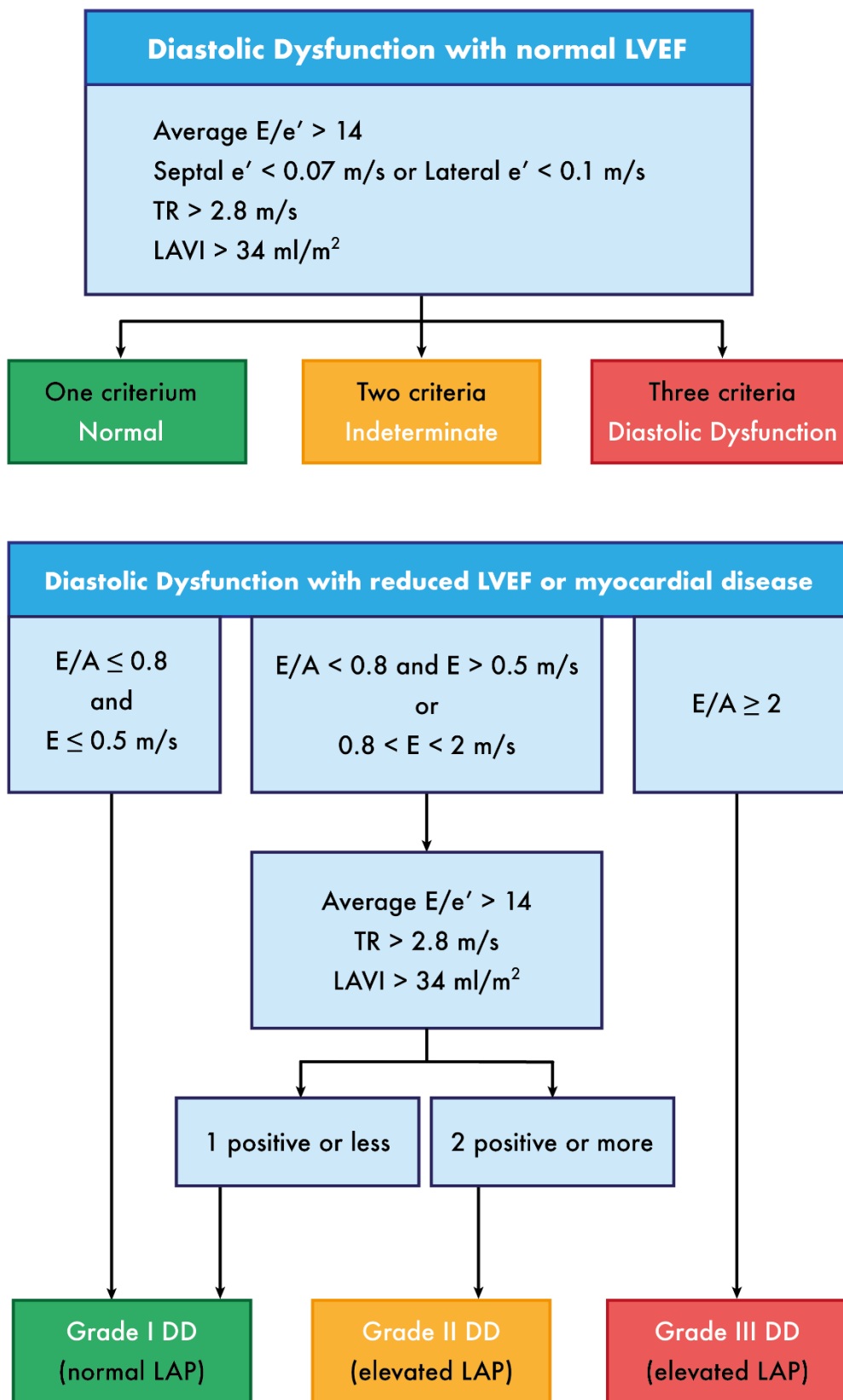
Figure 10 – Diagnostic algorithm for DD in patients with normal or reduced LVEF/myocardial disease as per the 2016 guidelines of the American Society of Echocardiography [71]. LVEF – left ventricular ejection fraction, TR – tricuspid regurgitation jet velocity, LAVI – left atrial volume index, LAP – left atrial pressure.

| Variable	Description	Physiological correlate
Table 3 – Main variables used to characterize diastolic function and grade diastolic dysfunction by echocardiography.		
Peak E-wave velocity (m/s)	Peak mitral inflow velocity in early diastole	LA-LV pressure gradient in early diastole
Peak A-wave velocity (m/s)	Peak mitral inflow velocity in late diastole	LA-LV pressure gradient in late diastole
E/A ratio	Peak E wave velocity divided by peak A wave velocity	LV filling pattern (normal, impaired relaxation, pseudo-normal or restrictive)
Septal and lateral e' velocity (m/s)	Mitral annular early diastolic velocity in the septal and lateral portion of the myocardium	Correlated with tau (LV relaxation rate)
E/e' ratio	Peak E wave velocity divided by average e' velocity	Predicts LV filling pressures and corrects for effect of LV relaxation on E-wave
Left atrial volume index (LAVI) (ml/m^2)	LA volume indexed to body surface area	Correlated with long-term elevation of LV filling pressures and independent predictor of death
Tricuspid regurgitation jet velocity (m/s)	Velocity of the tricuspid regurgitant jet, used to estimate TRPG	Correlated with left atrial pressure and representative of poorer prognosis if severely elevated
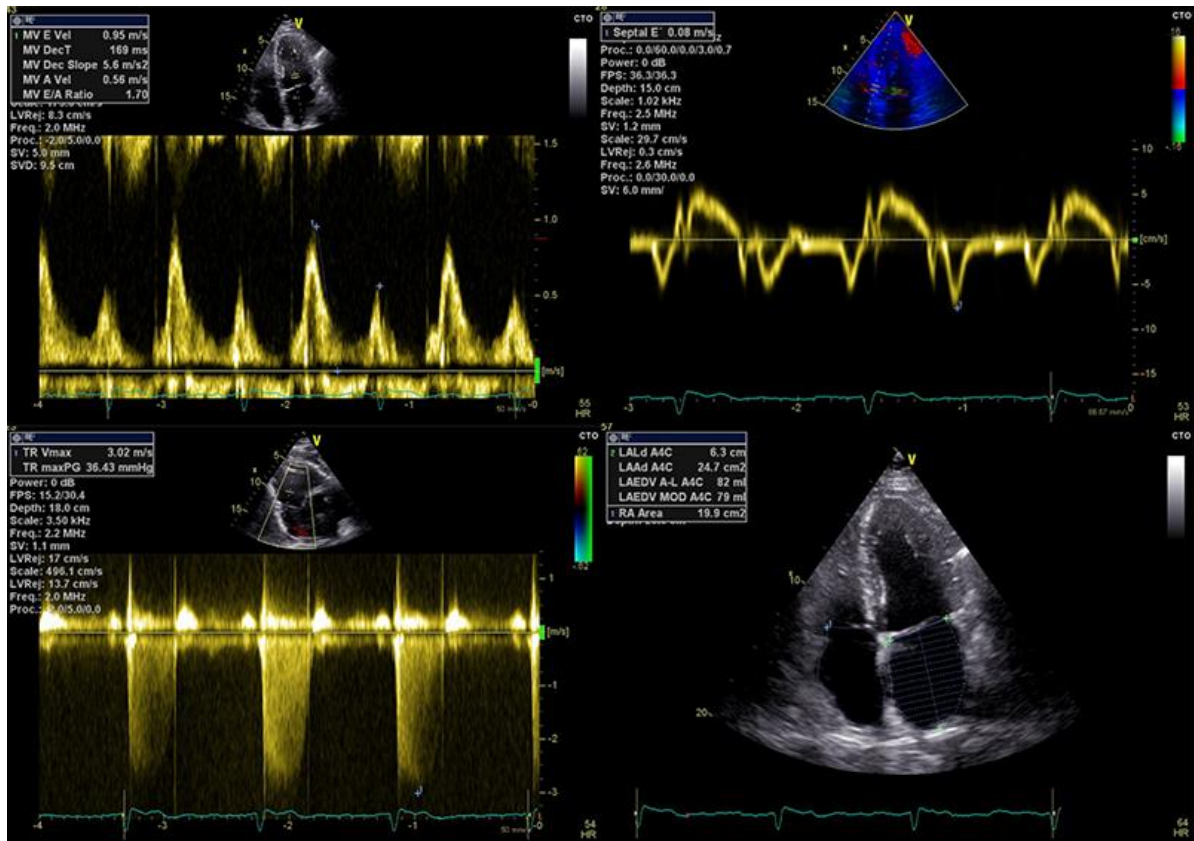
Figure 11 – How the main variables to assess diastolic parameters are measured with echocardiography. *Top left:* Measurement of E-wave and A-wave, with calculation of E/A ratio. *Top right:* Measurement of septal e' (lateral e' is measured in a similar way, but on the lateral portion of the myocardium). *Bottom left:* Measurement of TR, as detailed in the previous chapter. *Bottom right:* Measurement of LA volume and calculation of LAVI based on the patient's body surface area.

2.3.2 CMR

CMR is the reference method for non-invasive measurement of heart chamber mass and volume. It is also an adequate modality for measurement of LA volume and calculation of LAVI [79]. These CMR measures are important components of diastolic function assessment. In CMR, LA volume is can be calculated via the area-length method, which is analogous to the area-length method by echocardiography.

Regarding transmitral flow and myocardial annular velocities, CMR has shown worse performance, mainly due to lower temporal resolution than echocardiography [80]. While the literature shows previous attempts at acquiring these variables with CMR with acceptable correlation with echocardiography measurements, there has been an underestimation of the values by a considerable margin. This has presented as an opportunity to attempt to develop CMR flow measurements techniques with higher temporal resolution that are later described in this thesis.

Pulmonary flow can reliably be assessed by CMR, but PA pressure is not routinely measured. As TR, and by extension TRPG, by echocardiography are estimates of systolic PA pressure, CMR methods such as the ones described in the previous chapter [26] could prove useful also for the assessment of diastolic function.

Newer CMR techniques, such as myocardial tagging [81] and elastography [82], have shown utility in the diagnosis of diastolic dysfunction. The former allows for detailed characterization of myocardial movement during the cardiac cycle (strain, strain rate, deformation), which could potentially translate into myocardial stiffness. The latter produces stiffness maps based on mechanical wave propagation in the myocardium. These methods are fairly recent and would benefit from technical advances to facilitate their use.

Since no comprehensive CMR method for assessment of DD is available that is comparable to the ones relying on echocardiography, one of the aims of Study V was to develop and validate such a method, which is further described in the forthcoming section.

3 CARDIOVASCULAR MAGNETIC RESONANCE

"Any sufficiently advanced technology is indistinguishable from magic."
in Profiles of the Future (1962)*, Arthur C. Clarke*

3.1 BASIC PRINCIPLES

Magnetic resonance imaging (MRI) is a process by which hydrogen protons that constitute the human body are induced into producing a signal that can be read and processed into an image. MRI has numerous applications in Physics, Chemistry and Medicine.

Atomic nuclei of uneven mass number (such as hydrogen, which only has one proton) possess an angular momentum, or *spin*. Conceptually, this means that they are spinning spheres with a small electrical charge. If subject to a strong external magnetic field B_0, the magnetic momentum vector resulting from the spin is given by the equation:

$$\omega = \gamma B_0 \qquad\qquad (7)$$

where ω is the precession frequency (also called the Larmor frequency) and γ is the gyromagnetic ratio of the nucleus (a known constant for each element) [83].

In any given tissue sample, the average angular momenta of all spins is called net magnetization vector (NMV), i.e. a single vector can describe the magnetic properties of all spins. At thermal equilibrium, the NMV is aligned with B_0. If these spins are subject to another magnetic field B_1, induced by a radiofrequency (RF) pulse tuned to the Larmor frequency of that specific element, they manifest the resonance phenomenon. This magnetic field B_1 excites the spins and its presence induces an oscillation (precession) that produces a signal that can be measured. MR cameras include receptor coils that receive this signal and then produce electrical current, based on the Faraday Law of electromagnetic induction.

When B_1 is turned off, relaxation of the spins occurs. There are two components to relaxation – a longitudinal one (in relation to B_0), in which an increase in magnetization in the longitudinal direction takes place characterized by T1, and a transverse one, in which there is a decrease in magnetization in the transverse plane, orthogonal to the B_0 direction, characterized by T2. T1, or spin-spin relaxation time, refers to the time necessary for the longitudinal component to reach 63% relaxation. T2, or spin-lattice relaxation time, refers to the time necessary for the transverse component to decay to 37% signal. T1 and T2 are both important parameters probed by MR pulse sequences to achieve images with desired properties or image contrasts.
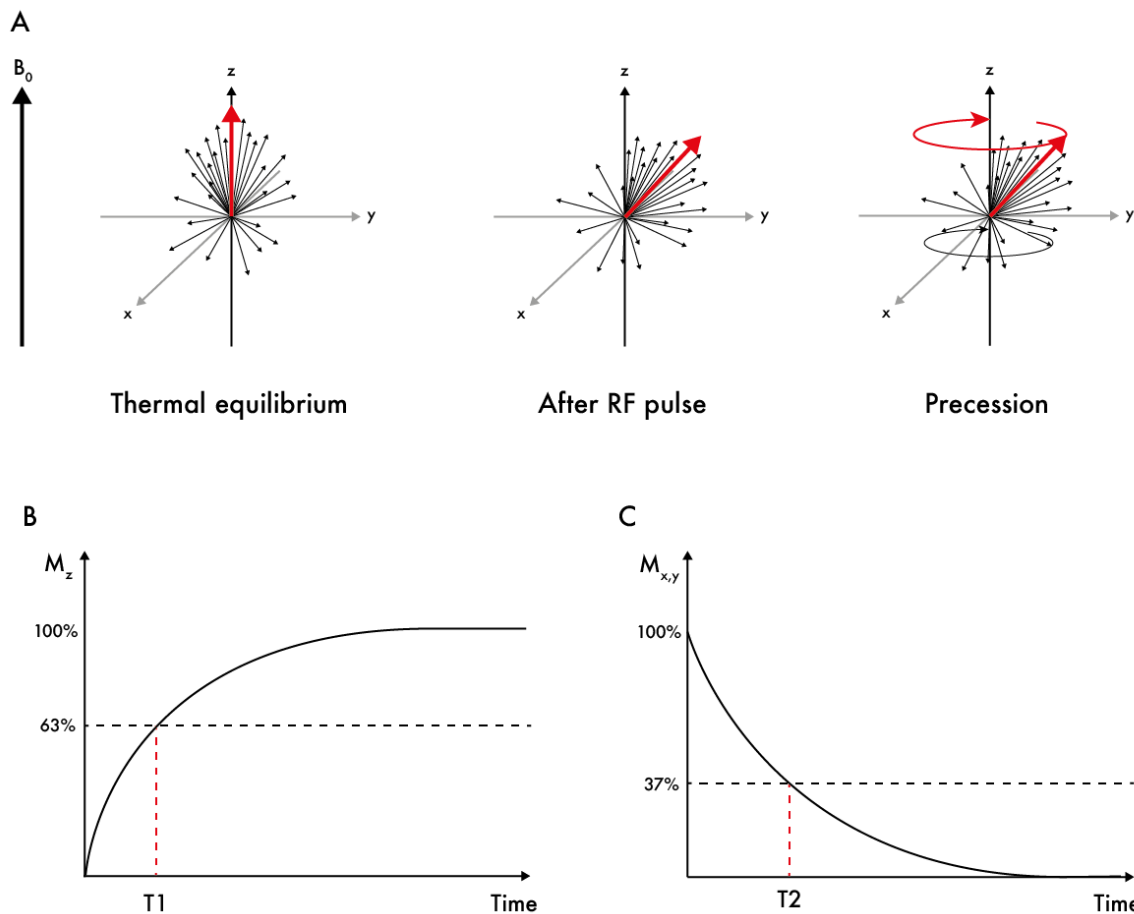
Figure 12 – A: Simplified schematic demonstration of how magnetic fields and RF pulses influence spins. At thermal equilibrium, the NMV (red arrow) is aligned with B_0. The RF pulse causes a deviation from the z axis in a certain angle (flip angle). After the RF pulse and until relaxation, the individual spins precess (black circular arrow) and therefore the NMV also precesses (red circular arrow). B: Magnetization in the longitudinal direction after the RF pulse plotted across time, signaling T1 as the time point corresponding to 63% relaxation. C: Magnetization in the transverse plane after the RF pulse plotted across time, signaling T2 as the time point corresponding to a decay to 37% signal.

If one irradiates the human body with an RF pulse, all the excited spins will precess at the Larmor frequency, making it impossible to receive a signal from a specific volume or portion of interest in the body. To solve this problem and achieve spatial encoding, i.e. image a specific volume, gradient magnetic fields are employed, which feature varying magnetic field strengths along a given direction *x*. The result is a gradient of Larmor frequencies along the direction *x*, which allows to isolate specific locations according to their specific Larmor frequency. Three gradients for each of the spatial directions (G_x, G_y, G_z) may be employed to position a slice.

After a slice is selected, one needs to be able to distinguish different signals along the directional axis, so that an image can be reconstructed. Along the short anatomical axis, the signal is located by means of a phase encoding gradient. Phase, along with frequency, is one of the fundamental characteristics of a signal. A phase encoding gradient temporarily causes a phase shift along the short axis, so that, when the next gradient is turned on (frequency encoding), different spins along the short axis of the image will have different accumulated phase shifts.

Along the long anatomical axis (in any projection, axial, coronal or sagittal), the process to locate the signal is called frequency encoding, which employs yet another magnetic gradient to shift the precession frequency of the spins along its axis.
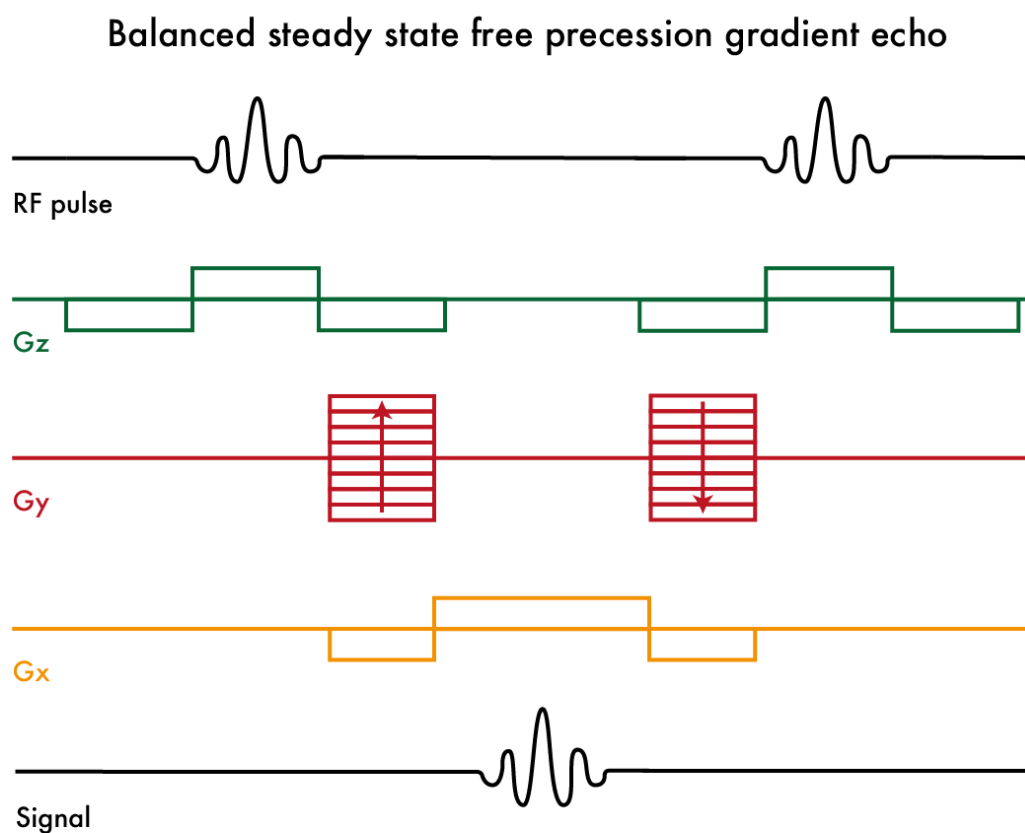

Figure 13 – Diagram of the sequence structure of balanced steady state free precession (bSSFP). RF – radiofrequency, Gz – slice selection gradient, Gy – phase encoding gradient, Gx – frequency encoding gradient.

Each data point, composed by frequency and phase information, is stored in a matrix called *k-space*. This includes all of the MR image data in the frequency domain. To convert k-space into an image readable by a clinician, one applies an algorithm called Fast Fourier Transform (FFT). There are mathematical aspects to this algorithm that are outside the scope of this

thesis; in summary, because of FFT, each pixel of the final image takes frequency and phase information from all the pixels in k-space and is assigned a tone on a greyscale.

In MRI, the RF pulses and gradients (as well as their timings) constitute a pulse sequence, as exemplified in Figure 13. A pulse sequence allows the operator to choose which imaging parameters should be applied depending on which images will be acquired. The balanced steady state free precession (bSSFP) pulse sequence [84], as shown on Figure 13, was frequently used in this thesis' studies to acquire anatomical images and cine stacks (e.g. for measurement of LV volume), whereas flow measurements were performed with a velocity encoded gradient echo (GRE) pulse sequence.

3.2 CLINICAL APPLICATIONS

CMR imaging is regarded as the most accurate modality in the assessment of myocardial morphology and function [85]. In the last few decades, image quality has dramatically improved. Currently, this allows for the non-invasive assessment of myocardial tissue characteristics and hemodynamic variables without exposure to ionizing radiation.

A basic CMR exam begins with scout imaging, for simple anatomical evaluation of the heart and thorax, as well as determination of the long and short-axis views. Cine imaging is then used for global and regional evaluation of the LV and/or RV wall motion, mass and ejection fraction. A short-axis cine stack is used to segment the LV in its epicardial and endocardial components and derive LV function parameters, as shown in Figure 14 [86].

By employing contrast agents such as gadolinium, one may assess myocardial perfusion during the cardiac cycle, which is increasingly relevant in patients with ischemic heart disease. Moreover, late gadolinium enhancement imaging, which is acquired 10-15 minutes after contrast injection with inversion-recovery sequences, allows to further characterize myocardial tissue, both in ischemic heart disease, cardiomyopathy, sarcoidosis and cancer [87].

Lastly, velocity encoding MR imaging of blood flow can be used to assess hemodynamics in blood vessels, cardiac valves and shunts. In the clinical routine, it is common to measure aortic and pulmonary flow, by using 2D phase-contrast MR. In this thesis, the featured methods were flow measuring techniques that expand the current clinical capabilities of MR. LV characterization with cine-imaging was also performed in all studies.
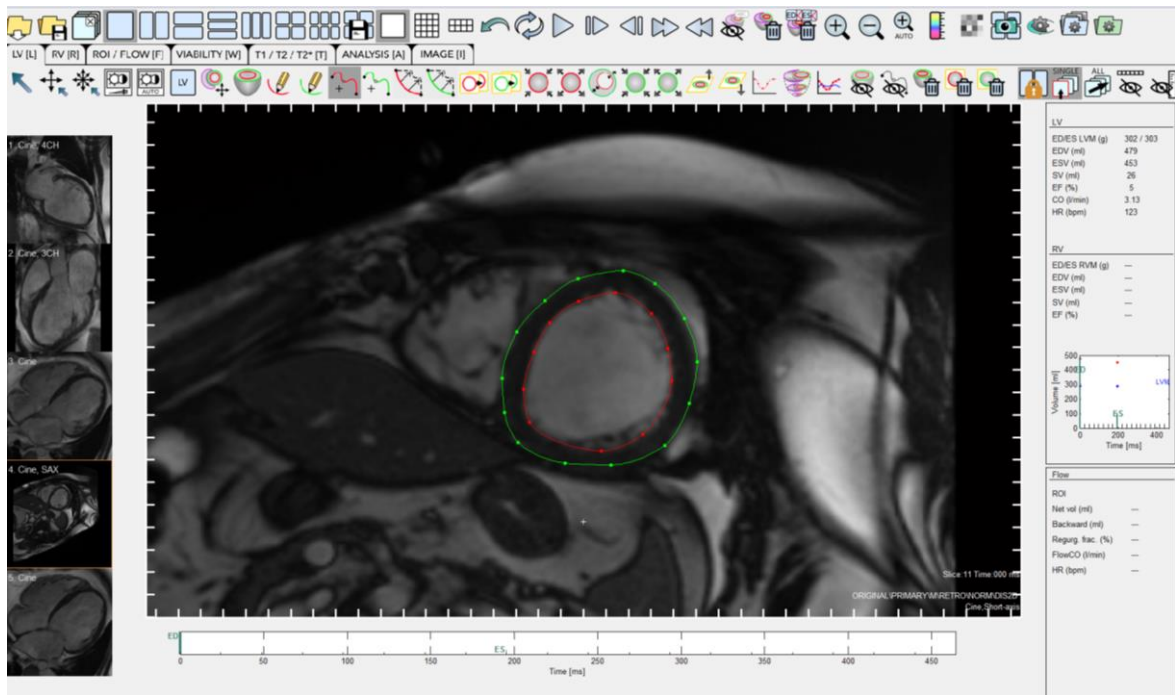
Figure 14 – LV segmentation in the open-source software suite Segment (Medviso, Lund, Sweden). The green and red lines correspond to the epicardium and endocardium respectively, isolating the myocardium from the rest of the image. This segmentation is performed on all images of a cine short-axis stack. The analysis yields values for myocardial mass, end-systolic and -diastolic volumes, ejection fraction, stroke volume and cardiac output.

3.3 FLOW MEASUREMENT METHODS

3.3.1 2D Phase Contrast MRI

A complete evaluation of cardiovascular function requires the assessment of blood flow in selected vessels or heart chambers. Heart valve function may be impaired by stenosis or regurgitation, and shunt identification is essential when evaluating congenital heart disease. CMR, particularly 2D Phase Contrast MR, allows the user to quantitatively assess blood flow, by measuring stroke volume, blood flow velocity, vessel area change, regurgitant flow, and other variables [88].

Phase contrast MRI exploits the fact that phase shifts of moving spins are proportional to their velocity. This way, not only is it possible to distinguish between static and moving spins, but also to quantify through-plane velocity in a given direction in each pixel in the image. Concurrently, spins moving at a similar velocity and opposite directions have similar but opposite phase shifts.

To create a phase shift, slices are sequentially subject to a flow-encoding gradient after excitation and before read-out, along spatial directions *x* and *y*. Flow-encoding gradients consist of sequential bipolar gradients, which causes spins that move in its direction to gain phase. Flow-encoding sequences require the operator to define the *velocity encoding gradient*, or more commonly VENC, which corresponds to the maximum velocity encoded by the sequence. If the true velocity one is measuring is greater than VENC, *aliasing* will occur, yielding false velocity readouts. On the other hand, always defining high VENC will not solve the problem, as it may considerably decrease velocity-to-noise ratio (VNR), resulting in poor measurement precision with regards to velocity.

3.3.2 Sector-wise golden-angle phase contrast (SWIG)

2D phase contrast MR is routinely used to measure blood flow in a time-resolved fashion, across several R-R intervals. However, diastolic flow variables (E, A, e') can only be measured in a very short window of maximal velocity, during a single heartbeat. Doppler echocardiography offers temporal resolutions that allow the measurement of these variables, but routine CMR methods do not [80]. There have been previous attempts to measure diastolic flow parameters with CMR, albeit with limited results.

Study IV documents the development and validation of a sector-wise golden angle (SWIG) radial profile ordering phase contrast sequence that attempts to solve this problem by enabling high temporal resolution. Instead of the classic Cartesian k-space ordering, SWIG divides k-space into several radial sectors corresponding to a pre-determined number of heartbeats (Figure 15). A golden-ratio division of the sectors is then performed as follows:

$$\emptyset_{n+1} = mod\left[\left(\emptyset_n + \frac{\pi}{N} \cdot \frac{\sqrt{5}-1}{2}\right), \frac{\pi}{N}\right] + s \cdot \frac{\pi}{N} \tag{8}$$

where s is the current heartbeat, N is the total number of heartbeats, and $\emptyset_n$ is the *n*th azimuthal angle [89].

Compared to Cartesian ordering, the SWIG method presents several advantages, such as sampling the center of k-space in every TR, linear sampling density, and considerable undersampling that allows high temporal resolution, at the expense of spatial resolution.

Reconstructed SWIG images are analyzed in Segment (Medviso AB, Lund, Sweden) [90] and are compensated for eddy current-dependent phase error with quadratic phase error correction. Semi-automated phase unwrapping is also applied. Transmitral and myocardial tissue velocities are measured using an in-house developed plugin, which allows to choose the image voxel was the highest velocity in either the mitral opening (for transmitral velocities) or mitral annulus (for septal and lateral myocardial tissue velocities).
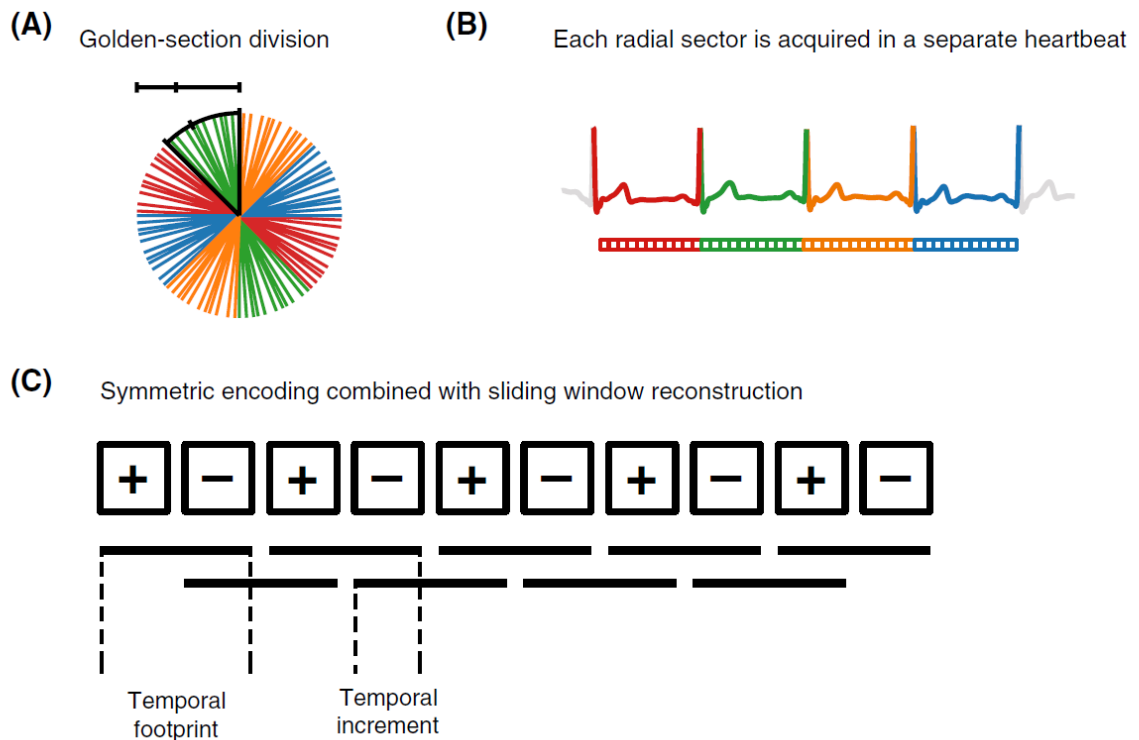
Figure 15 – Visual representation of the technical aspects of the SWIG method. A – k-space spokes are established by performing a golden-angle division of each sector. B – k-space sectors are acquired in a single corresponding heartbeat. C – Each k-space spoke is acquired with alternating positive or negative VENC using a sliding-window technique. Each square represents an image with either positive (+) or negative (-) VENC. Each line (temporal footprint) represents a pair of positive or negative VENC frames that compose a phase-contrast image. Reproduced from Fyrdahl, *et al*. (2020) with permission.

Figure 16 – Comparison between transmitral and myocardial tissue velocities measured with TTE (A and B) and SWIG CMR (C and D). The measurements were performed in a patient with grade I DD. Image reproduced from Fyrdahl, *et al*. (2020) with permission.
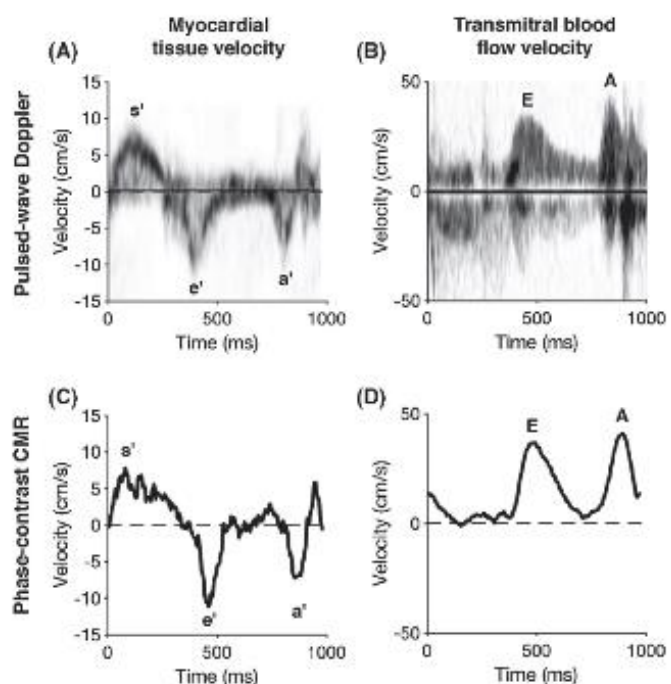
3.3.3 4D Flow Analysis

In Studies II, III and V, a 4D flow analysis vortex duration method [25] [26] was employed to diagnose PH and estimate mPAP. With this method, flow data in the pulmonary artery is acquired with 6-10 gapless slices of a 2D spoiled-gradient-echo-based cine phase contrast sequence, with VENC 90 cm/s in all three spatial directions, and retrospective ECG gating. Images are acquired in approximately an oblique sagittal orientation optimized to cover the pulmonary trunk. The result of the acquisition is an image of stack of 20 frames, with a three-dimensional overview of flow in the pulmonary artery during one cardiac cycle (Figure 17).
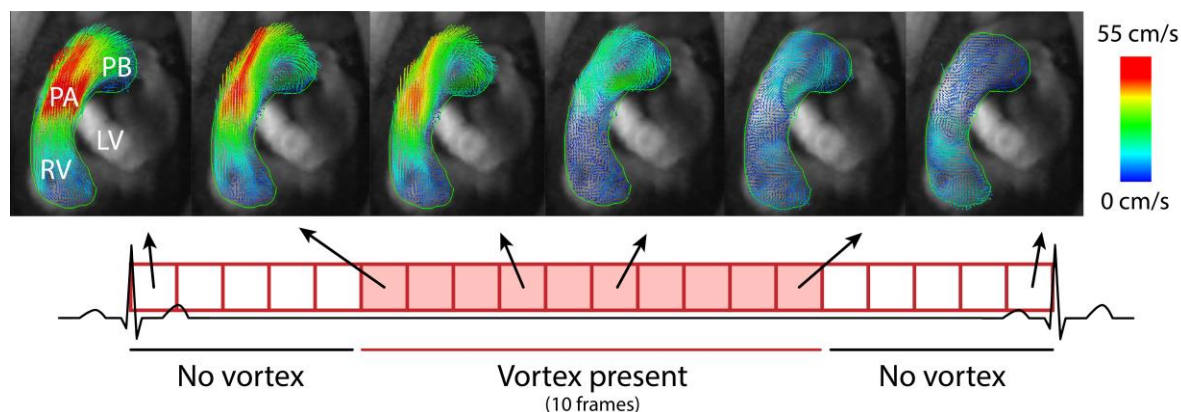

Figure 17 – Frame count with a PH vortex in the cardiac cycle. Out of 20 total frames comprising one cardiac cycle (R-R interval), only images from six frames are shown as pointed by the arrows. A total of 10 frames (pink boxes) had a PH vortex. The white boxes represent frames without a vortex. A vortex duration of 10/20 timeframes (50% of the cardiac cycle) corresponds to a mPAP of 47 mmHg. RV – right ventricle, LV – left ventricle, PA – pulmonary artery, PB – pulmonary bifurcation. Color scale denotes velocity of blood flow. Reprinted with permission from Ramos JG, *et al.* (2020).

Image analysis consists of automatic background phase correction and phase unwrapping. Images are then manually segmented to isolate the right ventricular outflow tract and seed 3D vectors. Vortex analysis per se usually begins with an overview of pulmonary artery flow in streamline visualization. This initial view allows the observer to identify several potential vortical formations: (1) a PH vortex, which usually starts inferiorly and slightly distal to the pulmonary bifurcation, (2) a bifurcation vortex, composed mostly of helical flow and present in most healthy individuals, and (3) a pulmonary valve vortex, which is usually more pronounced in patients with an incompetent pulmonary valve [25].

Additionally, a PH vortex must obey a set of criteria that strongly point to it being in fact representative of PH and not a normal helical structure, such as a bifurcation vortex. A true PH vortex:

- Is composed of notional closed concentric curves (Figure 18), which reflect the nature of a circular vortex with a well defined center,

- Starts in mid- to late-systole and ending in early- to mid-diastole, which rules out smaller low velocity vortices sometimes observed in late-diastole, and,
- Is characterized by a moving center, as PH vortices usually start in the inferior portion of the main PA and gradually move towards the center of the artery.

Vortex duration expressed as a percentage of the cardiac cycle is measured by counting how many consecutive timeframes in which these criteria apply, and then dividing by the total number of timeframes. mPAP is then calculated by applying the previously described empirically determined equation [26]:

$$mPAP_{CMR}(mmHg) = \frac{Vortex\ duration\ (\%) + 25.44}{1.59} \tag{9}$$

Increased PA pressure by CMR is defined as vortex duration $\geq 10\%$, which corresponds to an invasively measured mPAP > 22 mmHg.
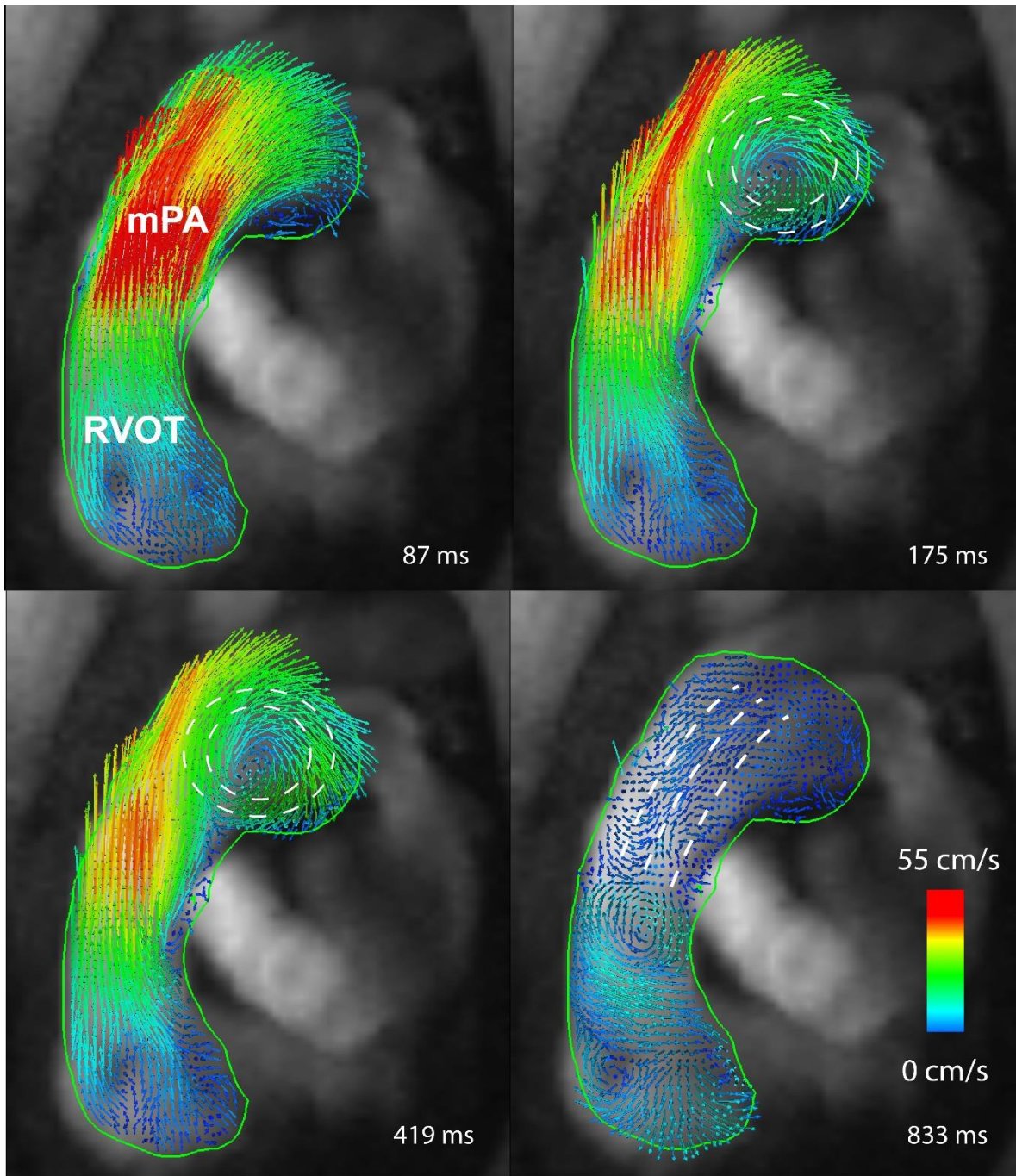
Figure 18 – Vortex visualization during one cardiac cycle in a 3D velocity vector view in a multi-plane reformatted sagittal slice. Top left: no PH vortex is visualized in early systole. Top right and bottom left: a PH vortex is visualized as noted by the white notional concentrical curves, with a clear vortical center. Bottom right: no vortex visualized in the main PA, as noted by the lack of concentrical curves. Time in milliseconds (ms) denotes time after the R-wave trigger of the ECG. RVOT – right ventricular outflow tract, mPA – main pulmonary artery. The color scale denotes velocity of blood flow.

4 COMPARISON BETWEEN DIAGNOSTIC METHODS

"THE ARCHITECT: Your life is the sum of a remainder of an unbalanced equation inherent to the programming of the Matrix. You are the eventuality of an anomaly, which despite my sincerest efforts I have been unable to eliminate from what is otherwise a harmony of mathematical precision."

in The Matrix Reloaded (2003)*, L. and L. Wachowski*

4.1 GENERAL CONSIDERATIONS

In Medicine, diagnostic tests are tools to gather data – usually physiological variables – with the purpose of making a clinical decision. When developing new diagnostic tests, the researcher must prove that the new test is at least non-inferior to the existing ones through statistical testing.

The unifying theme in this thesis has been the development of new CMR methods to diagnose disease or estimate variables that are already routinely assessed by other diagnostic modalities. A crucial step in the validation of these new techniques has been the comparison of the diagnostic performance of the new methods with the reference methods, as established by the current recommendations.

4.2 ACCURACY AND PRECISION

Evaluating the quality of a diagnostic test involves consideration of two aspects – precision and accuracy (Figure 19). Precision refers to the reliability of the test, i.e. the degree to which the test's result varies with repeated measurement. On the other hand, accuracy refers to the validity of the test, i.e. the degree to which the test's result matches the true value of the target variable [91].

Assessing reliability (precision) is done by calculating intra- and inter-observer variability, which express how much repeated testing alters the result if done by one rater or a second rater, respectively. In both cases, two sets of measurements are compared with each other, either in absolute terms or as a percentage. This is further detailed in section 4.4 below.

As far as accuracy is concerned, one intends to know how does the test's result compare to the gold standard measurement. For example, if testing the accuracy of a screening test for prostate cancer, the gold standard would be biopsy, since biopsies usually establish the true

diagnosis with a very high degree of certainty. Accuracy is also related to sensitivity and specificity of a test, which are described in the next section.
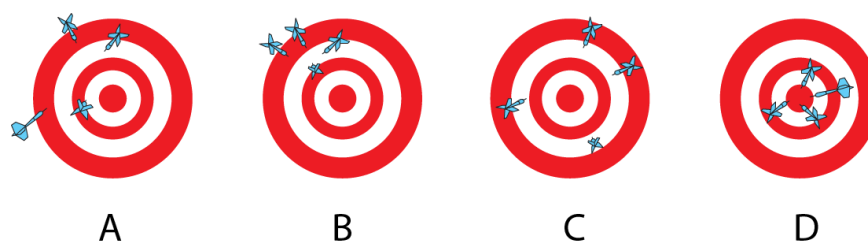

Figure 19 – Target grouping to graphically represent accuracy and precision. A – Inaccurate and imprecise. B – Precise but not accurate. C- Somewhat accurate, but imprecise. D – Accurate and precise. Image used under a Creative Commons license CC BY-SA 3.0, by cleanpng, Wikimedia Foundation.

These traditional definitions of accuracy and precision are not without caveats. If no clear gold standard can be defined, for example in the case of subjective scales, it is difficult to define accuracy. On the other hand, if we consider precision to be only one of the components of reliability, as defined mathematically, intra- and inter-observer variability are not enough to define precision. For the purposes of the studies presented in this thesis, however, the definitions above are acceptable.

4.3   SENSITIVITY AND SPECIFICITY

Only rarely do diagnostic tests detect the presence or absence of disease in nearly 100% of cases. On the contrary, the varying performance with regards to diagnostic accuracy must be considered when interpreting the results of any test to make correct clinical decisions. Similarly, no set of symptoms are always present in a certain syndrome. This is true even for those who are regarded as being classic symptoms or pathognomonic.

The proportion of positive or negative test results that represent presence or absence of disease, respectively, can be plotted in a 2x2 contingency table as shown in Table 4.

Sensitivity is defined as the probability that a certain test yields a positive result in a patient who has the disease. In clinical terms, sensitivity is useful to estimate the capability of the test in ruling out disease, since a test with high sensitivity will yield few false negatives.

Specificity is defined as the probability that a certain test yields a negative result in a patient who does not have the disease. Clinically, specificity is useful to estimate how well a test rules in disease, since a test with high specificity will yield few false positives.

Table 4 – Contingency table for evaluation of diagnostic performance of a test

		Disease		
		Present	Absent	
Test	Positive result	True positive (TP)	False positive (FP)	$\text{PPV} = \dfrac{TP}{TP+FP}$
	Negative result	False negative (FN)	True negative (TN)	$\text{NPV} = \dfrac{TN}{TN+FN}$
		$\text{Sensitivity} = \dfrac{TP}{TP+FN}$	$\text{Specificity} = \dfrac{TN}{TN+FP}$	$A = \dfrac{TP+TN}{TP+TN+FP+FN}$

PPV – positive predictive value, NPV – negative predictive value, A – accuracy
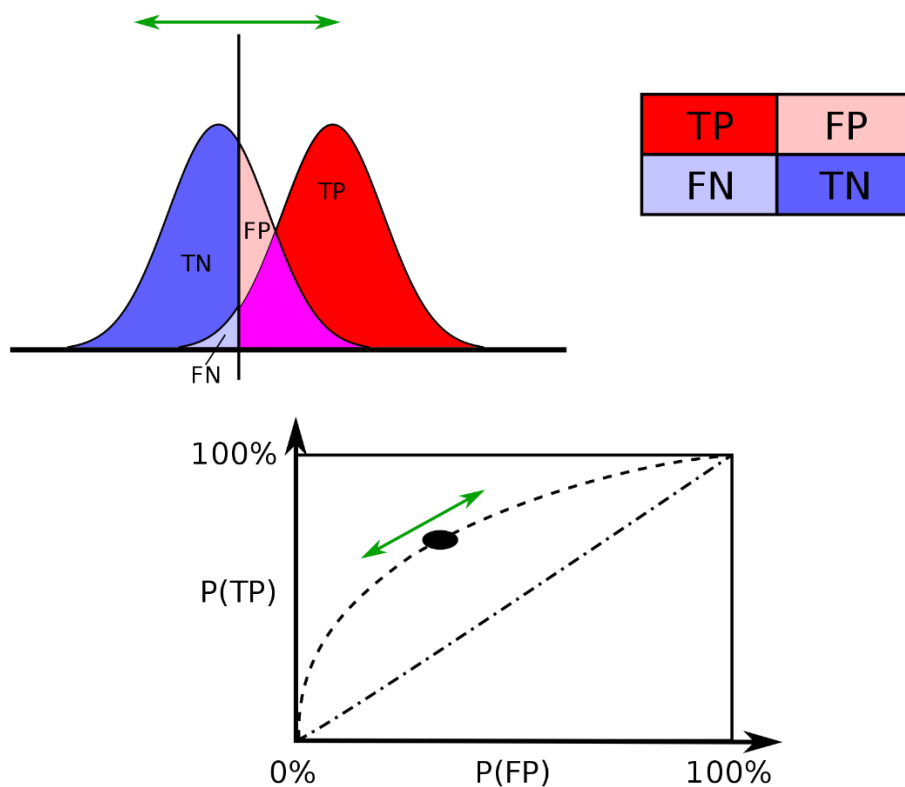

Figure 20 – Graphical explanation of sensitivity, specificity and ROC curves. The green arrows represent the decision threshold for a test – moving it along the horizontal axis will always increase sensitivity and decrease specificity or vice-versa. By plotting sensitivity against the false positive rate, one can identify the cut-off threshold that maximizes the test's accuracy. P(TP) – sensitivity, P(FP) – false positive rate or 1-Specificity. Image licensed under a Creative Commons license CC BY-SA 3.0, created by Sharpr, Wikimedia Foundation.

Accuracy, in the context of contingency tables, specificity and sensitivity, is dependent on all four variables in the table and is defined as the test's ability to correctly differentiate between presence or absence of disease.

To avoid arbitrary cut-offs in a given test, the optimal cut-off threshold for a test is established by analyzing a receiver operating characteristic (ROC) curve, which plots sensitivity against false positive rate, i.e. the probability of getting a true positive result against the probability of getting a false positive result. The optimal threshold is the one that confers the optimal combination of a high sensitivity and a low false negative rate (and therefore high specificity). The integral of this curve (area under the curve) is also an indicator of the diagnostic performance of the test, and may be used as a composite comparison of sensitivity and specificity between tests. However, in some situations, sensitivity and specificity may not be weighted equally, e.g. if the cost of a false positive outweighs the cost of a false negative, or vice-versa. In these cases, other approaches to determining ideal cut-off values are appropriate.

4.4 STATISTICAL METHODS

These previous basic concepts pave the way to assessing agreement between two diagnostic modalities, which was done in several studies in this thesis, either comparing CMR with RHC or CMR with echocardiography. We intended to answer essential questions in these studies – whether the results of a test would remain the same if evaluated by two different operators (therefore being precise) or by two different methods (therefore being accurate).

Agreement between two continuous variables can be evaluated using linear regression, if it is hypothesized that a linear relationship between them will be observed. In linear regression, the value of R^2 (correlation coefficient) can be interpreted as the extent to which one variable is predicted by the other in a linear fashion. Moreover, the equation resulting from the regression may be extracted from a testing cohort and then tested in a validation cohort to assess how well the testing variable predicts the outcome variable.

Bland-Altman analysis is also useful as a measure of the pattern of agreement and for assessment of bias. A Bland-Altman chart (such as the one in Figure 25, right panel) is plotted with the mean of both variables in the horizontal axis and their difference in the vertical axis [92]. The Bland-Altman plot also shows the 95% limits of agreement, with an upper and lower limit of agreement defined by mean difference ± 2 standard deviations respectively. Such a plot can also identify the presence and frequency of outliers.

As mentioned previously, comparing the area under the curve of two ROC curves is a direct comparison of the accuracy of two diagnostic tests performed on the same patient. This

comparison is performed with the DeLong test, to account for the correlation between the data, i.e. to compare two areas under the curve that were computed from the same patient cohort [93].

Table 5 – Procedures for agreement analysis.		
Number of variables	**Type of variable**	**Procedure**
Two	Categorical	Cohen's kappa Weighted kappa McNemar's test
	Numerical	Intraclass correlation coefficient Lin's concordance correlation coefficient Bland-Altman plot Paired t-test British Standards reproducibility coefficient
Three or more	Multivariate analysis	

Adapted from Watson PF et al. (2010) [94].

For categorical variables, agreement may be reported as agreeable cases as percentage of total cases. This simple proportion does not, however, account for the effects of chance, particularly when the number of total categories is small. This can be accounted for by calculating Cohen's kappa, which factors in the probability of getting an agreement by chance [95]. The resulting index lies between -1 and 1, with values closer to one representing higher agreement. The unweighted Cohen's kappa is applied in 2x2 contingency tables, while the weighted variant is used when there are 3 or more ordered categories.

5 AIMS

"Far away there in the sunshine are my highest aspirations."
in Little Women (1868)*, Louisa May Alcott*

The general aim of this thesis was to explore the potential of both routine and innovative CMR methods in the diagnosis of heart failure and PH. Given the rising accessibility and technical capabilities of CMR, there is an interest in expanding its diagnostic scope, since diastolic dysfunction and PH are not currently routinely assessed with CMR.

For each study specifically, the aims were:

- **Study I:** To investigate normal pulmonary vascular physiology and how different measures, including blood flow distribution and PBVV, vary with body position,

- **Study II:** To independently test and validate CMR mPAP estimation from 4D flow analysis vortex duration, compared to echocardiography TR,

- **Study III:** To independely test and validate CMR mPAP estimation from 4D flow analysis vortex duration, compared to invasive measurements by right heart catheterization,

- **Study IV:** To develop a high temporal resolution phase contrast pulse sequence for evaluation of transmitral blood flow and myocardial tissue velocities, and to compare it with TTE, and,

- **Study V:** To test the feasibility of a comprehensive CMR method for diagnosis and grading of diastolic dysfunction, compared to transthoracic echocardiography.
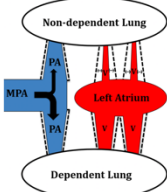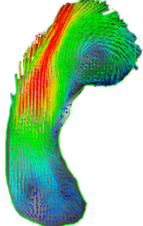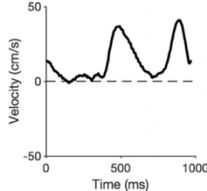
6 METHODS

> "You know my methods, Watson. Apply them."
>
> *in The Sign of the Four* (1890), by Sir Arthur Conan Doyle

6.1 STUDY DESIGN

This doctoral thesis focused on using CMR techniques to study normal pulmonary vascular physiology, and to evaluate diagnostic measures from CMR relevant to PH and DD. Table 6 – Diagram of study design for the present thesis, including the main object of study of each paper and the main physiological variables of interest. below summarizes the rationale behind each study and how they all fit into the big picture.

Table 6 – Diagram of study design for the present thesis, including the main object of study of each paper and the main physiological variables of interest.

Object of study		Diagnostic modality	Physiological parameters	Study
	Normal pulmonary vascular physiology	CMR 2D-PC	PA flow PBVV PVDR	Study I
	Non-invasive estimation of PA Pressure	CMR 4D Flow Echocardiography RHC	CMR mPAP Echo TR Invasive mPAP	Study II
				Study III
	Diagnosis and grading of diastolic dysfunction	CMR 4D Flow CMR SWIG Echocardiography	E and A velocities, E/A e' velocities, E/e' PA pressure LAVI	Study IV
				Study V

CMR – cardiovascular magnetic resonance, 2D-PC – two-dimensional phase contrast, RHC – right heart catheterization, PBVV – pulmonary blood volume variation, PVDR – pulmonary vascular distensibility reserve, mPAP – mean pulmonary artery pressure, SWIG – sector wise golden angle, PA – pulmonary artery, LAVI – left atrial volume index

6.2 STUDY POPULATIONS

Study populations for studies II, IV and V consisted of clinical consecutive patients with indication to perform a CMR exam at the Karolinska University Hospital, Stockholm, Sweden. Studies I and IV included healthy volunteers who were recruited to perform MR scans and echocardiography at the same hospital. Study III included patients referred for RHC who also underwent echocardiography and CMR. Ethical approval was granted for all procedures in all studies, and all subjects timely provided written informed consent.

In **Study I**, 10 healthy volunteers were prospectively recruited to assess normal physiology related to pulmonary blood flow distribution and PBVV. The inclusion criteria were an age of 18-65 years old, no significant history of previous disease, and no contraindications to CMR. Exclusion criteria were abnormal ECG findings prior to MR scanning, arterial hypertension and pregnancy.

For **Study II**, we prospectively included 60 consecutive patients referred to a clinical MR exam, who also underwent a TTE within 60 days or less (6 [1-20] days between exams). If no contraindications to CMR or atrial fibrillation were observed, patients were considered for inclusion.

In **Study III**, we prospectively included 40 patients with referral to RHC who also underwent a CMR exam and a TTE, most of which had suspicion or diagnosis of PH (6 [1-12] days between CMR and RHC).

In **Study IV**, we included 10 healthy volunteers for an initial pilot study to assess temporal resolution who underwent CMR and TTE (24 hours or less of difference between exams). Thirty-five consecutive patients were then included to evaluate accuracy and precision of the method, who underwent both CMR and TTE (4 [2-15] days between exam dates).

In **Study V**, we included 46 consecutive patients referred to a CMR exam because of suspected or diagnosed cardiopulmonary disease, who also underwent TTE (3 [0-16] days between exams).

6.3 ETHICAL CONSIDERATIONS

Over the course of this doctoral work, several human subjects, both healthy volunteers and patients with cardio-pulmonary conditions, were included in our studies. Most subjects underwent CMR, echocardiography and even invasive procedures. This raised ethical questions that were considered early on; our conclusions are summarized in this section.

Some patients suited to be included in our studies suffered from complex clinical conditions, from severe heart failure to multisystemic auto-immune diseases, and thus their recruitment

could be especially sensitive from an ethical perspective. In this case, the process of informed consent played an important role to respect these patients' autonomy and to ensure that the patient understood (1) that extra medical procedures (such as CMR in Study III) were completely voluntary and solely part of a research endeavor, and (2) what the procedure consisted in, including its benefits, if any, and risks.

Fortunately, MR scans have few contraindications and do not involve emitting ionizing radiation. In accordance with principle 16 of the Declaration of Helsinki [96], we could therefore provide improved diagnostic information to our research subjects, while subjecting them to very limited risks. Furthermore, even with a limited perceived benefit of participating, the vast majority of patients were eager to take part in the research effort in a field of study that affects them daily.

Lastly, in the field of medical imaging research, there are frequent file transfers and processing of personal data, e.g. file transfer from the MRI scanner to image analysis computers and even personal research computers. These processes raise ethical questions, as images may carry personal data that is protected by law. A standard practice in the field, therefore, is to anonymize all images that are collected by the researcher. This process allowed safe transfer and processing of the image files, without the concern of violating the patients' rights as stated in the Swedish personal data law and the European Union's regulations.

6.4 CARDIOVASCULAR MAGNETIC RESONANCE

6.4.1 Basic CMR exam and LV Characteristics

All patients in all studies underwent a 12-lead electrocardiogram (ECG), blood pressure measurement and brief history to rule out contraindications to CMR. ECGs were acquired on a GE Marquette system (GE, Little Chalfont, United Kingdom).

All CMR images were obtained in either a Siemens Area 1.5T or Siemens Skyra 3T (Siemens, Erlangen, Germany) with ECG gating and phased array receiver coils.

The CMR protocol included a localizer sequence and 2-, 3-, 4- chamber balanced SSFP cine images of the left ventricle as well as a complete short axis (SA) stack. Typical image parameters included FOV 380x320 mm^2, matrix size 265x142 pixels with 1.5x1.5 mm^2 in-plane resolution, slice thickness 6 mm, bandwidth 930 Hz/Px, repetition time/echo time 2.78/1.16 ms, temporal resolution 36 ms interpolated to 35 cardiac phases per cardiac cycle.

LV parameters, which included LV volumes, mass and EF were measured from the cine short-axis stack using manual delineations in the software Siemens syngo.Via 4.1 (Siemens

Healthcare, Erlangen, Germany) or Segment (version 2.0 R5039, Medviso AB, Lund, Sweden) [90].

6.4.2 4D Flow Analysis

4D flow data in the pulmonary artery was acquired with 6-10 gapless slices of a commercially available retrospectively gated 2D spoiled-gradient-echo-based cine phase contrast sequence, with VENC 90 cm/s in all directions and threefold averaging to avoid breathing artifacts. Other protocol parameters included: FOV 340x276 mm^2, matrix 192x112 pixels, slice thickness 6 mm, bandwidth 449 Hx/Px, generalized autocalibrating partial parallel acquisition (GRAPPA) factor of 2, autocalibration signal (ACS) of 22 lines, flip angle 15°, TR/TE 6.41/4.10 ms, temporal resolution 77 ms interpolated to 20 cardiac phases per cardiac cycle, total imaging duration 6-11 minutes depending on heart rate and number of slices necessary to cover the main PA.

4D flow image analysis was then performed in prototype software Siemens 4D Flow (Siemens, Erlangen, Germany). Automatic eddy current compensation and phase-unwrapping were performed and images were segmented semi-automatically. Initial overview of the flow in the right ventricular outflow tract was performed in streamline mode. 3D vector visualization was then used to detect a blood flow vortex in the main pulmonary artery as previously described. As already described in Chapter 3, a vortex was considered pathological if (1) defined by notional concentric curves, (2) localized in the main pulmonary artery, and (3) beginning in early- to mid-systole. Vortex duration in percentage of the cardiac cycle was calculated based on how many frames the vortex could be visualized (out of a total of 20). mPAP was then estimated using the empirically determined equation describing the linear relationship between vortex duration and mPAP.

6.4.3 Step-wise Golden Angle (SWIG)

SWIG, as previously described, is a high temporal resolution step-wise golden-angle through-plane phase-contrast sequence which was developed in-house and validated against echocardiography in Study IV. SWIG uses a 150-250 frames/second sliding window, temporal footprint 40 ms and VENC 150 cm/s or 30 cm/s for transmitral and myocardial tissue velocities, respectively). Typical sequence parameters for transmitral flow included: FOV 320x320 mm^2, matrix size 64x64 pixels, bandwidth 1560 Hz/pixel, flip angle 20°, TE/TR 4.0/6.6 ms. Typical sequence parameters for myocardial tissue velocities included: FOV 320x320 mm^2, matrix size 64x64 pixels, bandwidth 1560 Hz/pixel, flip angle 8°, echo time/repetition time 4.4/6.8 ms.

Images were then analyzed in Segment (version 2.0 R5039, Medviso AB, Lund, Sweden) [90] expanded with a plug-in developed in house. Before velocity measurements,

compensation for Eddy-currents was applied using a quadratic fit to background stationary tissue.

6.5   ECHOCARDIOGRAPHY

Comprehensive transthoracic echocardiography was performed on all patients in studies II-V by an experienced operator using a commercially available system (Epiq, Phillips, Amsterdam, the Netherlands). Recordings were obtained from the left parasternal modified RV long axis, left parasternal short axis and apical four chamber views. All results were the mean of 3 measurements. TRPG in mmHg was calculated from TR jet velocity using the Bernoulli equation (4) as previously discussed. Increased PA pressure by echocardiography was defined as TR jet velocity > 2.8 m/s, corresponding to an estimated TRPG > 31 mmHg. Diagnosis and grading of DD was performed according to the recommendations of the American Society of Echocardiography and European Society of Cardiovascular Imaging.

6.6   STATISTICAL ANALYSIS

Statistical analysis was performed in Microsoft Excel 2016 (Microsoft, Seattle, WA, USA) and in the R-programming language in R-Studio 2.1 (RStudio, Boston, MA, USA). Continuous variables were reported as mean ± standard deviation if normally distributed per the Kolmogorov-Smirnov test, or median and interquartile range if non-normally distributed. Categorical variables were presented as percentages. In Study I, the Mann-Whitney U was used to perform comparisons between means of independent samples, and the Wilcoxon sign-rank test to compare means in paired samples. In the remaining studies, linear regression and Bland-Altman plots were used to compare the same measurements from different imaging modalities, as previously described in Chapter 4. Categorical agreements between DD grading methods in Study V was tested with Cohen's weighted kappa. A *p*-value of less than 0.05 was considered statistically significant in all studies.

7 RESULTS AND DISCUSSION

> "The game of science is, in principle, without end.
> He who decides one day that scientific statements do not call for any further test,
> and that they can be regarded as finally verified, retires from the game."
>
> *in The Logic of Scientific Discovery* (1934), Sir Karl Popper

7.1 NORMAL PULMONARY VASCULAR PHYSIOLOGY AND PBBV

In Study I, the main finding was the impact of gravity in blood flow distribution and pulmonary vascular distensibility. As shown in Figure 21, arterial blood flow distribution is shifted towards the dependent lung in the lateral position; in the supine position, we found a right/left distribution of 54%/46%, in contrast with 63%/37% in the right lateral position. The same held true for venous blood flow distribution (Figure 22), with the dependent lung draining more blood in the lateral position.
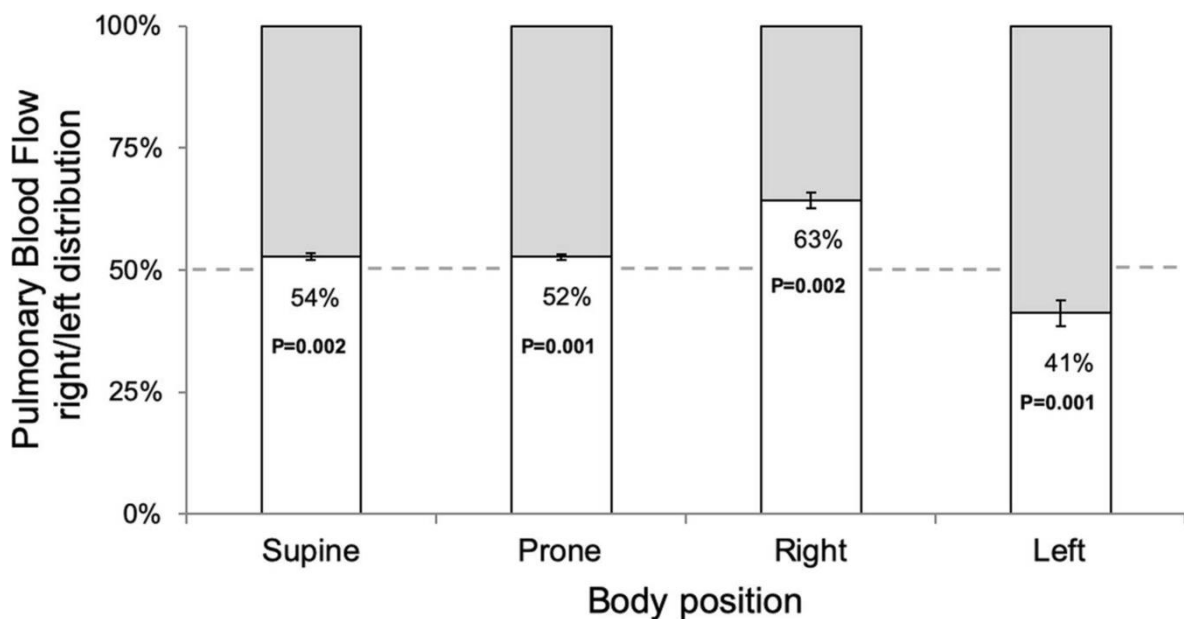
Figure 21 – Pulmonary blood flow distribution in each tested body position. The white bar represents the proportion of blood going to the right lung and the shaded bar represents blood going to the left lung. Error bars represent standard error of the mean. P-values yielded by a Wilcoxon signed-rank test with even distribution as null hypothesis. Reprinted with permission from Wieslander B, *et al.* (2019).

Before this study, there was no clear data on blood flow distribution in the pulmonary circulation in humans. Studies in dogs, primates and humans, as well as anesthesiology textbooks, suggested a right/left distribution of 55%/45% in the supine position and
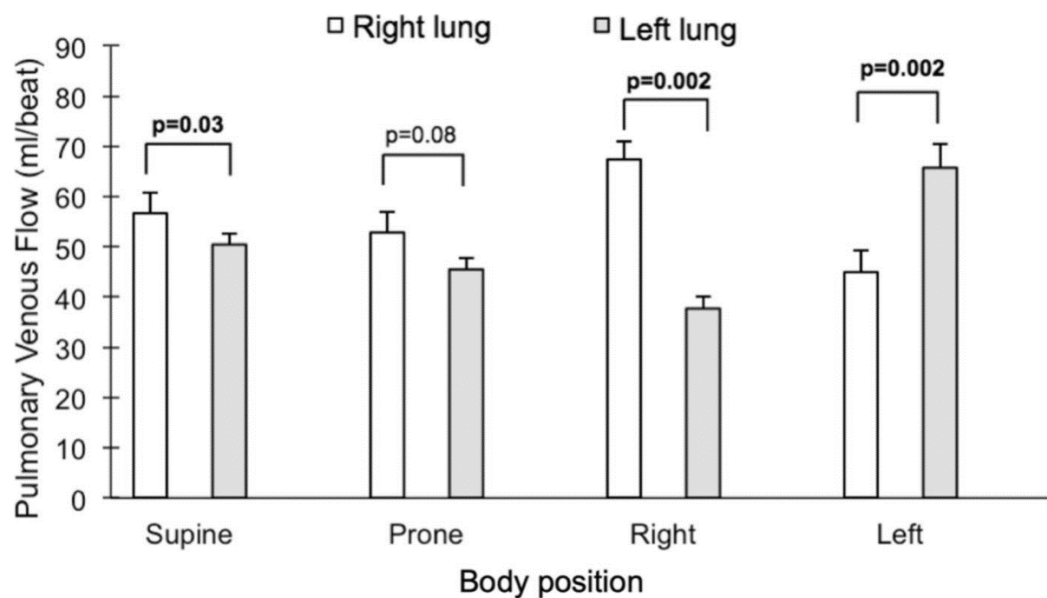
Figure 22 – Pulmonary venous blood flow volume from each lung in each tested body position. The white bars represent the right lung and shaded bars represent the left lung. Error bars represent the standard error of the mean. P-values yielded by a Wilcoxon signed rank test with no difference as the null hypothesis. Reprinted with permission from Wieslander B, *et al.* (2019).
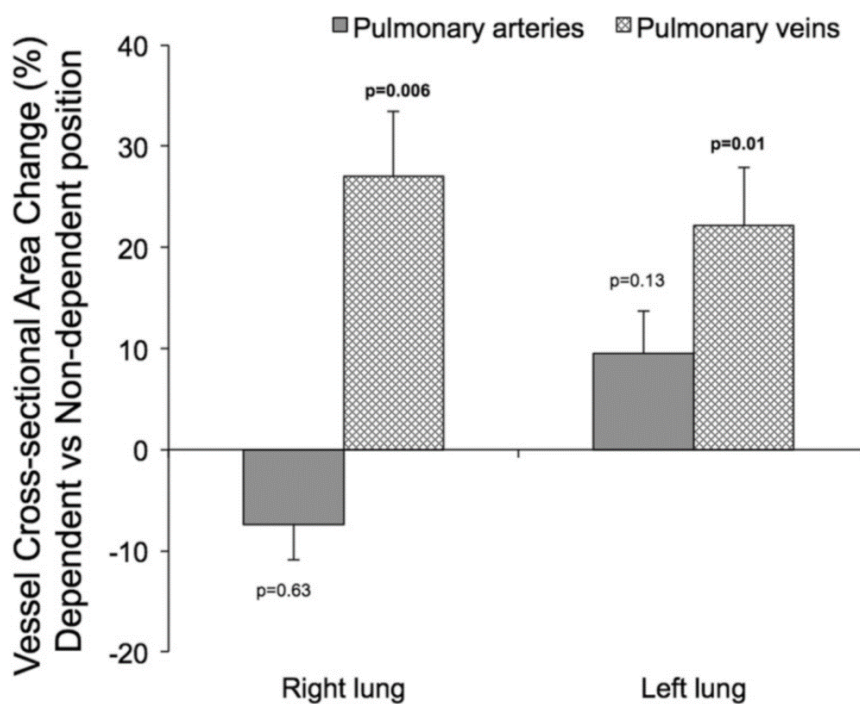

Figure 23 – Percent change in vessel cross-sectional area in the dependent position compared to the non-dependent position. The dark grey bars represent cross-sectional area change in arteries and the chequered bars represent area change in veins. The p-values refer to the hypothesis that the bars have a value different than zero, i.e. that there is a difference in cross-sectional vessel area when body position is changed. Reprinted with permission from Wieslander B, *et al.* (2019).

65%/35% in the right lateral position. All these studies consisted of small sample sizes and varying testing conditions (i.e. intubation, use of anesthesia, varying positive airway pressures). Study I was the first to use reliable and robust methods to investigate these research questions in a healthy human cohort breathing spontaneously.

In Figure 23, the relative cross-sectional area change of arteries and veins is shown. While relative arterial cross-sectional area did not vary between the non-dependent and dependent positions for either lung, venous cross-sectional area was higher in the dependent position compared to the non-dependent position in both lungs. These observations suggest that pulmonary veins distend considerably when under the effect of gravity in the dependent position, but the same is not true for pulmonary arterioles.
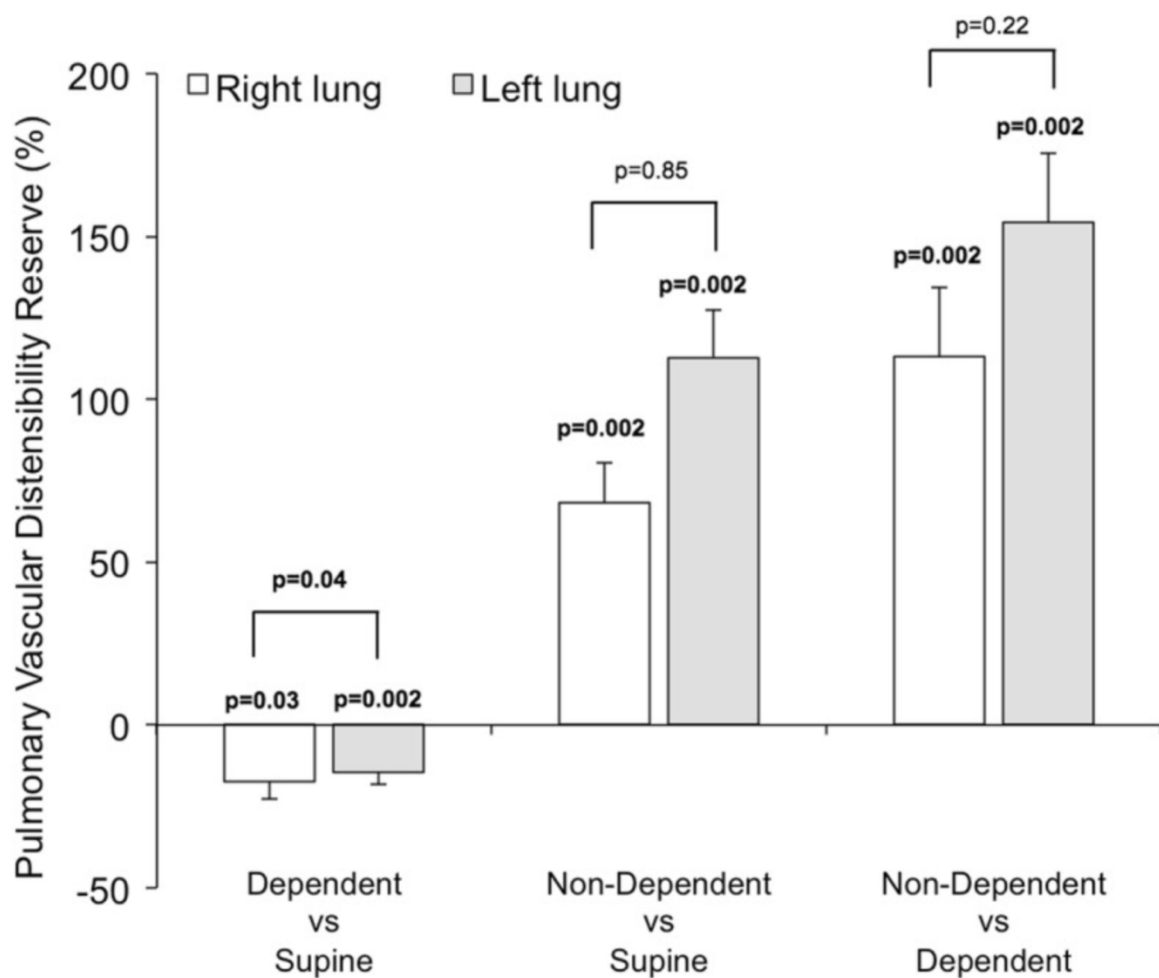

Figure 24 – Pulmonary vascular distensibility reserve (PVDR) changes with body position. PVDR is the relative PBVV change in the right lung (white bars) and left lung (grey bars). PVDR is greatly increased in the non-dependent lung on both sides. P-values directly above the bars represent the hypothesis that a bar has a non-zero value. P-values above brackets reflect the difference between the right and left lung. Reprinted with permission from Wieslander B, *et al.* (2019).

Unilateral PBVV as a percentage of unilateral stroke volume (relative PBVV) also varied with body position, with a 54% higher relative PBVV in the non-dependent left lung compared to the dependent right lung, as shown in Figure 24. This increase in relative PBVV in the non-dependent lung was termed lung pulmonary vascular distensibility reserve (PVDR). Considering a higher PBVV and a lower venous cross-sectional area in the non-dependent lung compared to the dependent lung in the lateral position, we suggest that PBVV is a measure inversely correlated with pulmonary venous distensibility. This is supported in part by previous findings that showed decreased PBVV in pigs with induced LV dysfunction, caused by a higher PCWP and consequent pulmonary venous distension [29].

Measurement of PBVV was shown to be reliable when measured by different observers, with an ICC of 0.89 for the left lung in the supine position and 0.98 for the left lung in the left lateral position. The Dahlberg error was 1.9 ml (relative Dahlberg error: 8.9%) and 1.2 ml (relative Dahlberg error: 3.5%), respectively.

7.2 DIAGNOSIS OF PULMONARY HYPERTENSION BY CMR

In Study II, 4D flow estimated mPAP by CMR with TR by echocardiography in a clinical consecutive population. In Study III, we compared 4D flow estimated mPAP by CMR with both RHC mPAP and echocardiography TR, in a clinical population referred to RHC due to suspected or confirmed PH. The main finding of both studies was that CMR mPAP correlates well with invasively measured mPAP, and moderately with echocardiography TR.

7.2.1 Estimation of CMR mPAP vs Echocardiography TRPG

Figure 25 shows a linear model comparing CMR mPAP and echocardiography mPAP and a Bland-Altman plot of the same measures, both in patients with both an observable TR and vortex duration greater than 15% of the cardiac cycle (corresponding to PH). We observed a good correlation ($R^2 = 0.65$, p<0.001) and low mean Bland-Altman bias of 4.0±6.9 mmHg.

As shown in Figure 26, CMR more than doubled the diagnostic yield of PA pressure estimation compared to echocardiography (35% vs 15%), i.e. CMR found that 35% of patients in this cohort had elevated PA pressure, in contrast with only 15% by echocardiography. Since a TR jet is not always obtainable [8] and previous studies showed discrepancies between echocardiography TR and invasive measurements of PA pressure [39], these findings may suggest that CMR has higher specificity for detection of increased PA pressure (which was also suggested by the findings in Study III).

These results assumed a right atrial pressure of 5 mmHg. RAP estimates from echocardiography were not used, since its estimation is known to result in poorer agreement [35].
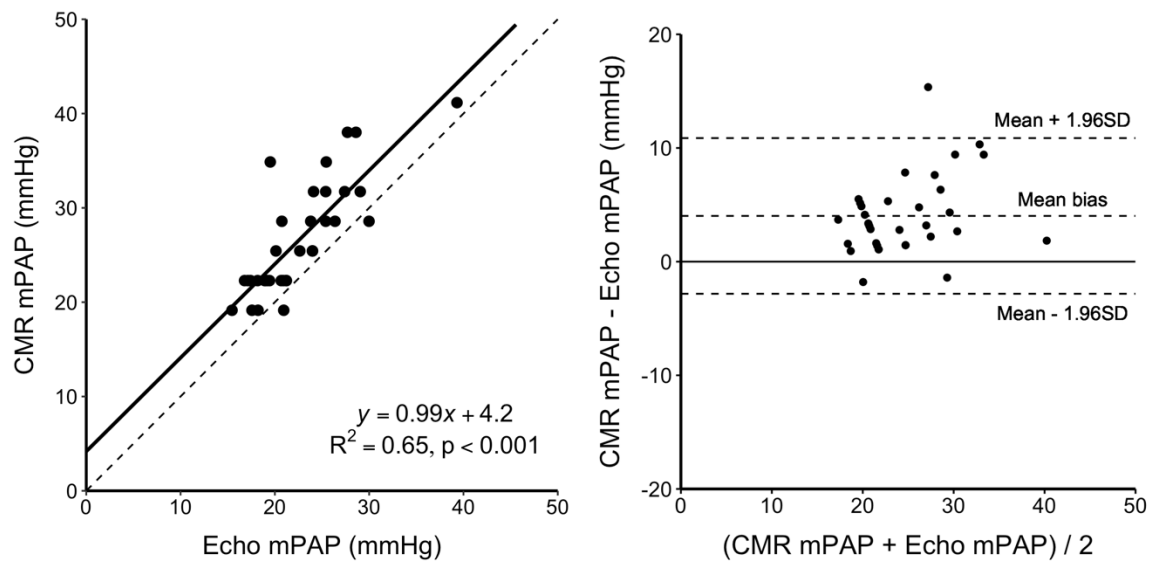
Figure 25 – Left panel: Linear regression (solid line) of estimated mean pulmonary artery pressure (mPAP) by CMR and estimated mPAP (Chemla equation) by echocardiography. Dotted line shows line of identity. Right panel: Bland-Altman plot of estimated mPAP by CMR and estimated mPAP by echocardiography in patients with both observable vortex and measurable TR. Mean bias 4.0±6.9 mmHg.
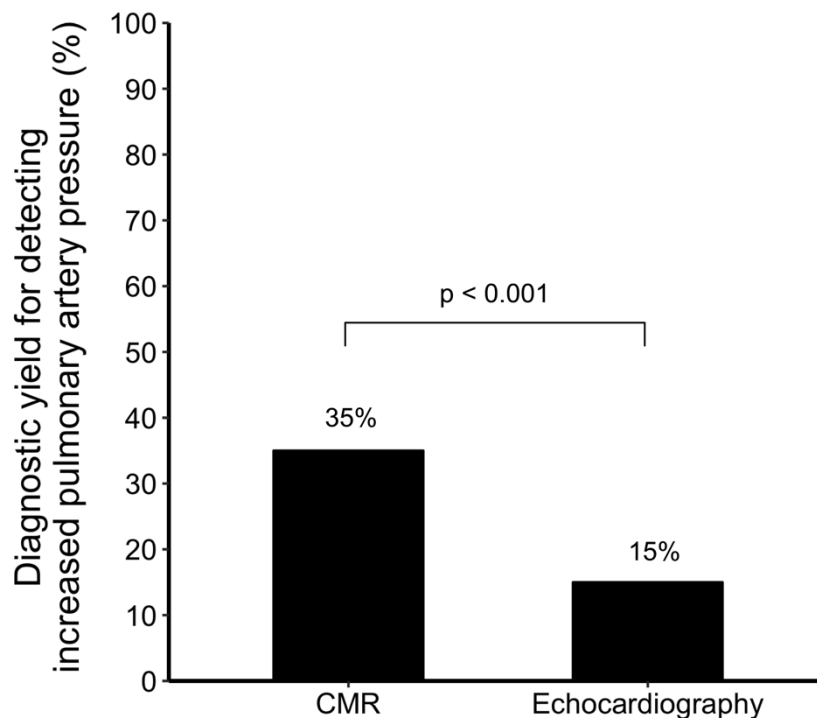

Figure 26 – Diagnostic yield for detecting increased pulmonary artery pressure by either a 4D flow pulmonary artery vortex duration > 15% of the cardiac cycle by CMR (corresponding to PH) or a tricuspid regurgitation jet velocity > 2.8 m/s by transthoracic Doppler echocardiography in all patients.

7.2.2 Estimation of CMR mPAP vs RHC mPAP

Figure 27 shows a linear model of CMR mPAP compared with invasive mPAP (left panel) and a Bland-Altman plot of the same measures (right panel). Estimation of PA pressure with CMR showed very good agreement with RHC (R^2=0.85) and low Bland-Altman bias of 1.3±4.7 mmHg. These results confirm the previous findings by the developers of the vortex method in an independent laboratory and different patient population. While the R^2 in this study was lower than in the first paper, mean Bland-Altman bias and regression parameters were similar [25] [26].
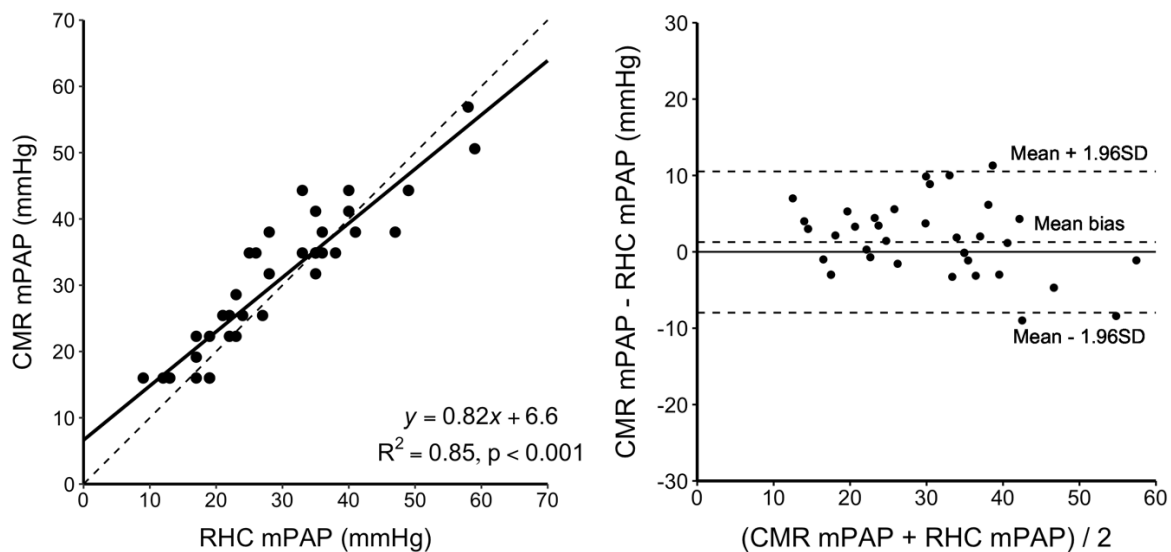
Figure 27 – Left panel: Linear regression (solid line) of estimated mPAP by CMR and mPAP by RHC. Dotted line shows line of identity. Right panel: Bland-Altman plot of estimated mPAP by CMR and mPAP by RHC. Mean bias 1.3±4.7 mmHg.

Compared to echocardiography, CMR showed higher sensitivity and accuracy, as well as higher correlation with invasive measures and lower Bland-Altman bias (Figure 28). CMR ruled out correctly all cases without PH (Table 7 and Table 8).

As mentioned in Chapter 1, there are other variables assessed by CMR that may aid in the diagnostic investigations in PH. However, none of them showed results comparable to the 4D flow analysis vortex evaluation method [88], which is thought to correlate directly with pulmonary vessel wall properties and compliance. 4D flow analysis shows the ability not only to diagnose PH, but also estimate PA pressure with a resolution of approximately 5 mmHg/frame and better diagnostic parameters than echocardiography. On the other hand, misidentification of vortices that do not fill the criteria listed in Chapter 3 may have led to false positives. This risk is minimized by proper training (preferably using a training dataset) and careful judgement of the properties of each vortex observed in the 3D volume.
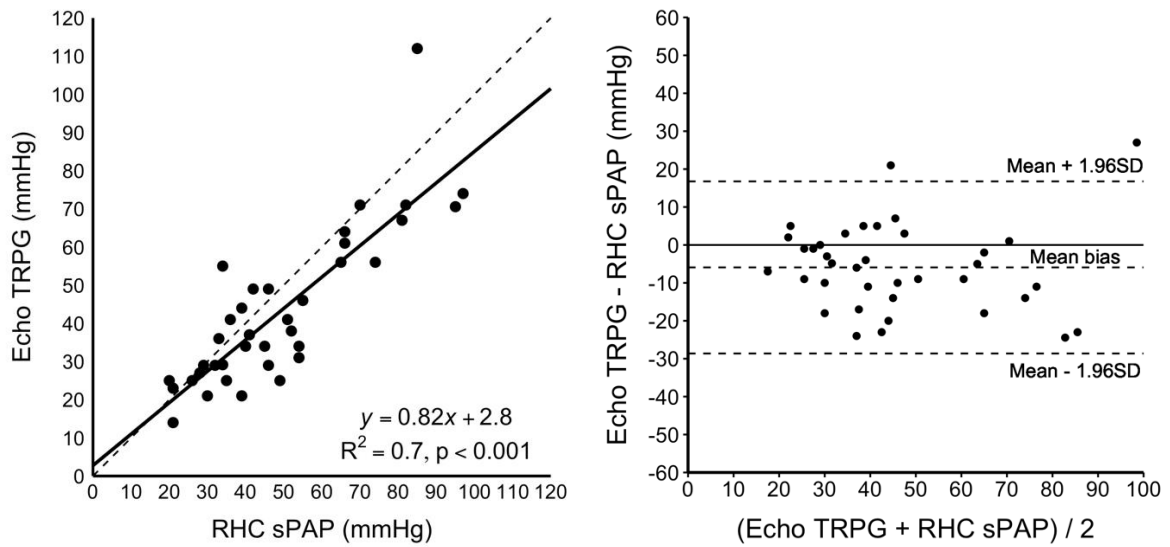
Figure 28 – Left panel: Linear regression (solid line) of TRPG by echocardiography and sPAP by RHC. Dotted line shows line of identity. Right panel: Bland-Altman plot of TRPG by echocardiography and sPAP by RHC. Mean bias -5.9±11.6 mmHg.

Table 7 – Contingency table for RHC vs echocardiography TR				
	Pulmonary hypertension			
Echo	Present RHC mPAP > 20 mmHg	Absent RHC mPAP > 20 mmHg	Total	
TR > 2.8 m/s	21 (56% true positives)	2 (5% false positives)	23	PPV = 91%
TR ≤ 2.8 m/s	6 (16% false negatives)	8 (22 % true negatives)	14	NPV = 57%
Total	27	10	37	

Sensitivity = 78%   Specificity = 80%   Accuracy = 78%

Table 8 – Contingency table for RHC vs CMR Vortex duration				
CMR	Pulmonary hypertension		Total	
	Present RHC mPAP > 20 mmHg	Absent RHC mPAP < 20 mmHg		
Vortex duration ≥ 10%	27 (73% true positives)	2 (5% false positives)	29	PPV = 93%
Vortex duration < 10%	0 (0% false negatives)	8 (22% true negatives)	8	NPV = 100%
Total	27	10	37	

Sensitivity = 100%   Specificity = 80%   Accuracy = 95%

7.3 DIAGNOSIS AND GRADING OF DIASTOLIC DYSFUNCTION BY CMR

7.3.1 SWIG Pilot Study

Study IV featured the development and validation of the SWIG sequence, which uses a radial sector-wise golden-angle profile ordering to acquire velocity information with very high temporal resolution, which is essential to correctly identify peak velocities of transmitral flow and myocardial tissue velocities.

In the first part of Study IV, different sets of SWIG image stacks with varying temporal footprints were acquired, based on the number of TRs – 4, 6, 8, 10 and 12. These images were compared with Doppler TTE to evaluate linear correlation and Bland-Altman bias, as shown in Table 9.

The second part of Study IV, which consisted in an in vivo patient study in clinical consecutive patients, showed good correlation ($R^2 = 0.63$, p<0.001) and low Bland-Altman bias of 0.009±0.037 m/s for myocardial tissue velocities. On the other hand, CMR underestimated transmitral velocities, with a Bland-Altman bias of -0.11±0.28 m/s and $R^2 = 0.45$, p<0.001 (Figure 29). This underestimation by CMR is, therefore, not likely due to insufficient temporal resolution, but image planning issues, specifically placement of the measurement slice and measurement volume. Further work is warranted to address this issue, as specified in Section 7.5.

Table 9 – Comparison between CMR SWIG-derived and TTE-derived myocardial tissue velocities (s', e', a') at a fixed temporal increment but a variable temporal footprint.

Temporal footprint (number of TRs)	Temporal footprint (ms)	Correlation (R^2)	Mean difference (m/s)	95% limits of agreement (± m/s)	*p*-value
4	27.2	0.46	0.01	0.043	0.03
6	40.8	0.63	0.009	0.034	0.13
8	54.5	0.72	0.004	0.030	0.41
10	68.0	0.69	-0.002	0.033	0.71
12	81.6	0.65	-0.009	0.035	0.14

P-value yielded by a Mann-Whitney U test with null-hypothesis that there was no difference between measurements. Reprinted with permission from Fyrdahl A, *et al.* (2020).
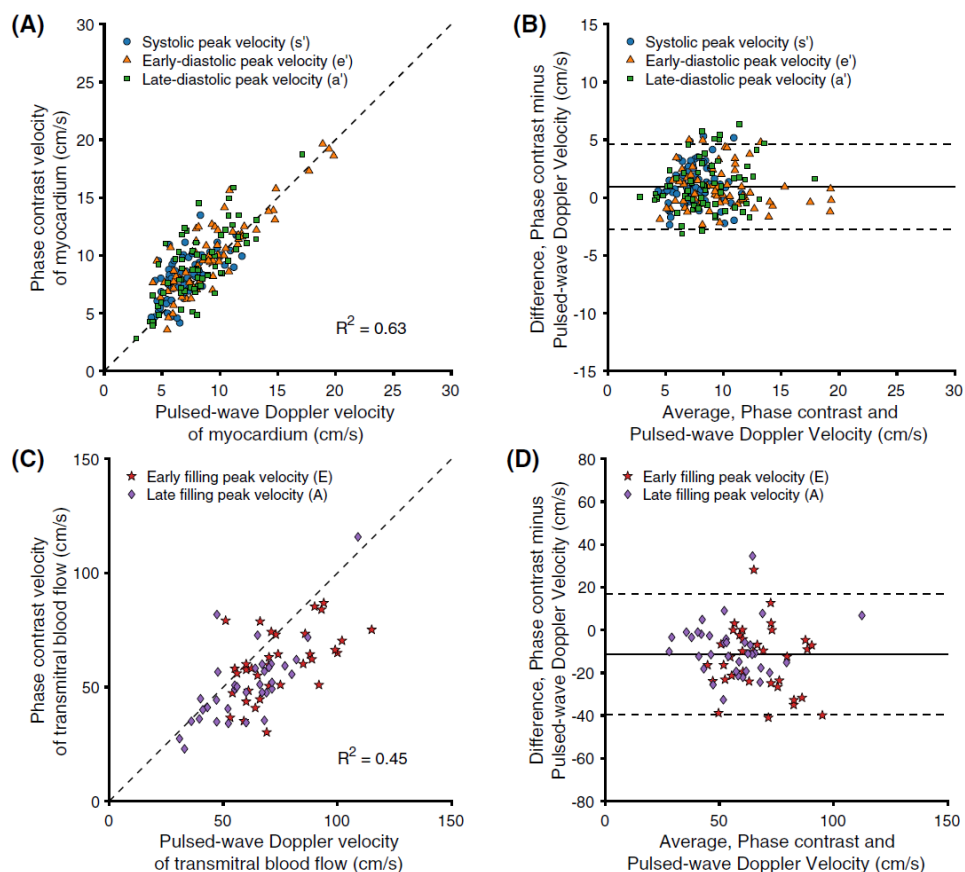
Figure 29 – A) Linear regression and B) Bland-Altman plot of myocardial tissue velocities measured with SWIG and Doppler TTE. C) Linear regression and D) Bland-Altman plot of transmitral velocities measured with SWIG and Doppler TTE. Reproduced with permission from Fyrdahl, et al. (2020). Reprinted with permission from Fyrdahl A, *et al.* (2020).

7.3.2 Comprehensive CMR Method for Diagnosis of Diastolic Dysfunction

Study V focused on the acquisition of three sets of data – (1) transmitral blood flow velocities (E, A, and E/A) and myocardial tissue velocities (septal e', lateral e' and average e') with the SWIG sequence; (2) LAVI with the biplane area-length CMR method (CMR BAL); and (3) estimation of mPAP with CMR 4D Flow analysis.

Figure 31 shows the linear regressions and Bland-Altman plots for measurement of transmitral and myocardial tissue velocities with CMR compared to Doppler TTE. While CMR systematically underestimated E velocities, the estimation of the E/A ratio yielded a good R2=0.87 (p<0.001) and low Bland-Altman bias of 0±0.15. This difference between the two modalities is likely do to issues related to planning of the measurement slice and measurement volume in CMR and not insufficient temporal resolution. Despite the lower agreement of E velocities, CMR still performed correct diagnoses, due to both E and E/A contributing to the algorithmic decision-making.

Estimation of mPAP with CMR showed similar results to the ones from Study II, with a comparable R2 and Bland-Altman bias (Figure 30). CMR showed again higher diagnostic yield than echocardiography in the estimation of elevated PA pressures.
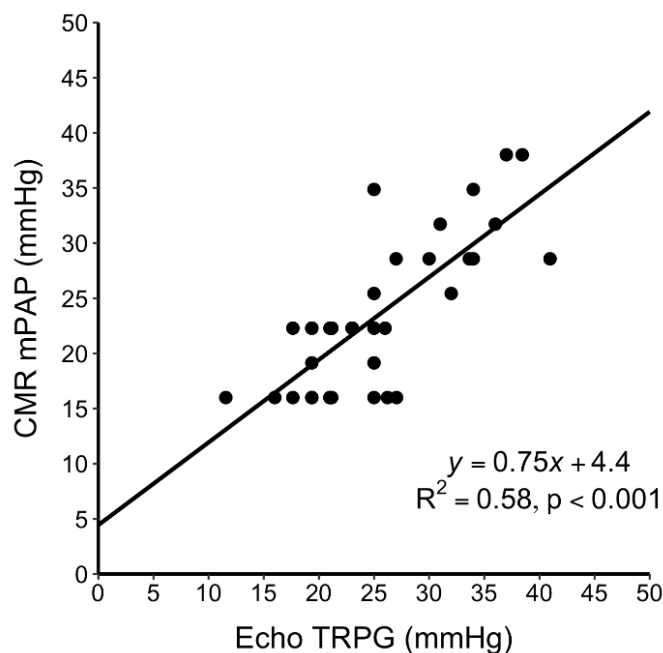

$$y = 0.75x + 4.4$$
$$R^2 = 0.58, p < 0.001$$

Figure 30 – Linear regression of the estimated mPAP by CMR and TRPG by echocardiography in patients with a measurable TR (n=37).

Concerning LAVI estimation, CMR measured higher LA volumes than echocardiography, which resulted in higher LAVI (Figure 32). These findings are in line with what other authors observed in studies comparing LAVI in CMR and echocardiography (CMR BAL vs echocardiography BAL) [97].
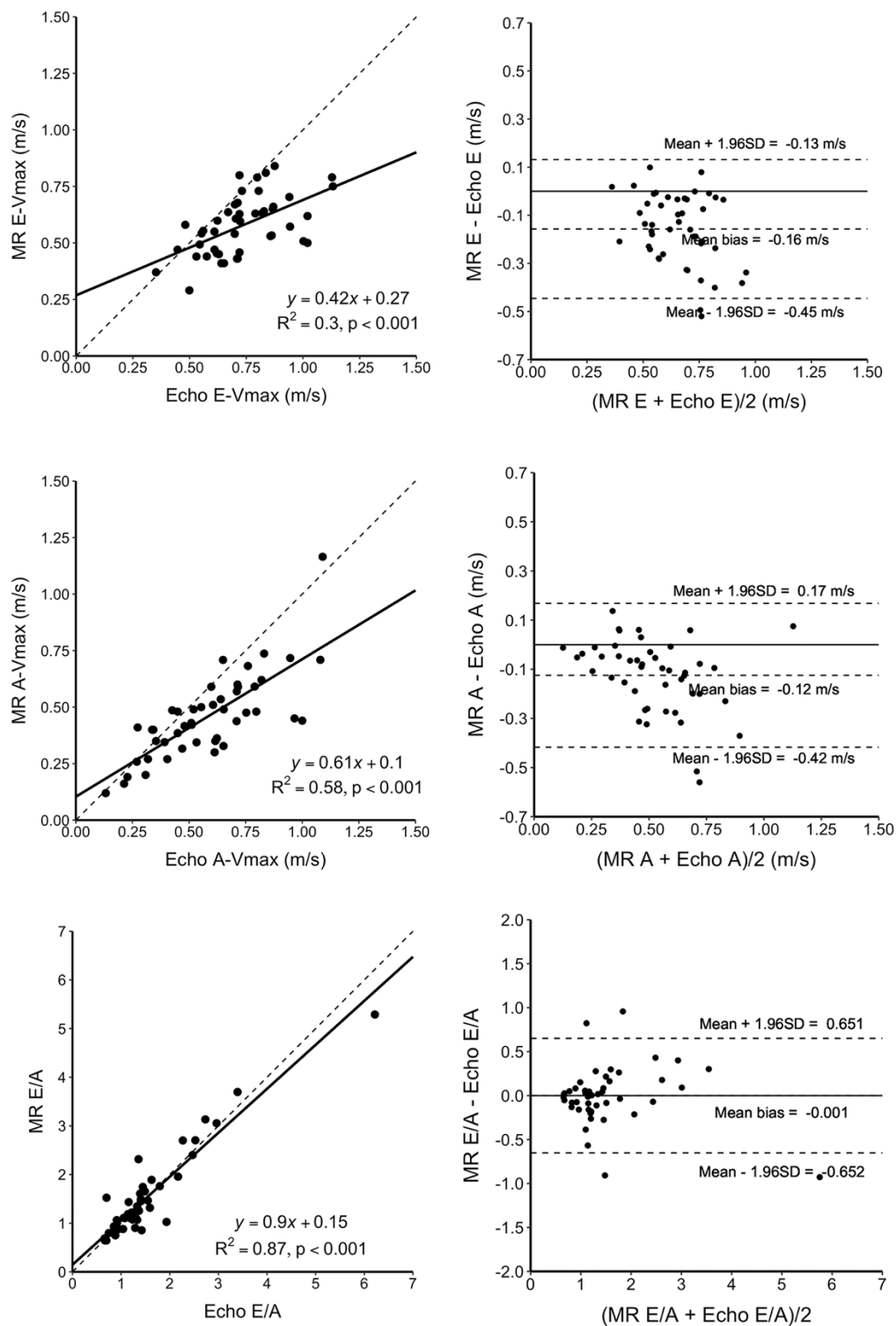
Figure 31 – Top left: Linear regression of the measurements of the peak E-velocity by CMR and echocardiography. **Top right:** Bland-Altman plot of the measurements of the peak E-velocity by CMR and echocardiography. **Middle left:** Linear regression of the measurements of the peak A-velocity by CMR and echocardiography. **Middle right:** Bland-Altman plot of the measurements of the peak A-velocity by CMR and echocardiography. **Bottom left:** Linear regression of the measurements of the E/A ratio by CMR and echocardiography. **Bottom right:** Bland-Altman plot of the measurements of the E/A ratio by CMR and echocardiography. Dotted lines denote the line of identity.
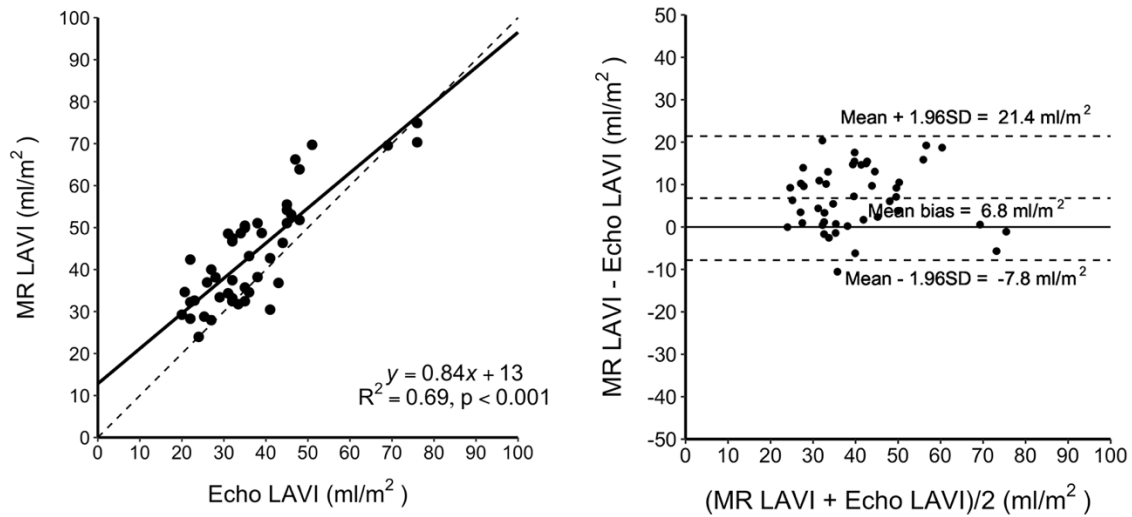
Figure 32 - **Left:** Linear regression of the measurements of left atrial volume index (LAVI) by CMR and echocardiography. **Right:** Bland-Altman chart of the measurements of the measurements of LAVI by CMR and echocardiography. Dotted lines denote the line of identity.

Table 10 – Agreement between CMR and echocardiography in the diagnosis and grading of diastolic dysfunction (blue cells represent agreement).

CMR \ Echo	Normal	Indeterminate	Grade 1 DD	Grade 2 DD	Grade 3 DD
Normal	3 (7%)	0 (0%)	0 (0%)	0 (0%)	0 (0%)
Indeterminate	1 (2%)	1 (2%)	0 (0%)	0 (0%)	0 (0%)
Grade 1 DD	0 (0%)	0 (0%)	25 (54%)	0 (0%)	0 (0%)
Grade 2 DD	0 (0%)	0 (0%)	4 (9%)	4 (9%)	0 (0%)
Grade 3 DD	0 (0%)	0 (0%)	1 (2%)	0 (0%)	7 (15%)

Overall, we observed excellent agreement between CMR and echocardiography (Table 10), with a percental agreement of 87% and a Cohen weighted kappa of 0.85 (95% CI: 0.73-0.97). In cases with disagreement, CMR always diagnosed DD as more severe than echocardiography, due to estimating either higher PA pressures or higher LA volumes. These results may suggest that CMR has a higher specificity for diagnosing DD than echocardiography, but studies with comparisons against invasive data would have to be performed to confirm this hypothesis.

7.4   STRENGTHS, LIMITATIONS AND FUTURE PERSPECTIVES

Phase-contrast CMR allows non-invasive measurement of flow and flow velocities with a high degree of accuracy and without the need for administering intravenous contrast agents. One of the general strengths of the studies included in this thesis was the study of flow with CMR, both in terms of flow velocity (peak transmitral velocities and PA flow, for example) and flow characteristics (PA vortex formation and duration), which directly correlated with physiological variables that influence clinical decision making.

Study I involved experiments related to normal physiology and while the sample size was appropriate to draw conclusions about PBVV and PVDR, one would need more healthy volunteers in order to establish normal values for those variables. Furthermore, while our inclusion criteria allowed for volunteers of all ages, the cohort ended up consisting of young subjects, which may not necessarily reflect the physiology of the older population. Additionally, while inter-observer variability was low for PBVV, it may be technically difficult to acquire adequate image planes from all four pulmonary veins which have varying anatomical positions and morphology.

Study II successfully applied the 4D flow analysis vortex duration method in a different lab than the one where it was developed. However, there were some limitations regarding the study population, as there was a difference between exam dates of maximally 53 days, with a median of 6 [1-20] days. This time difference may be associated with hemodynamic or clinical changes, yet several other comparative studies have allowed for even greater time differences with no significant impact on the data. Moreover, not all types of PH were present in this patient cohort, with a predominance of PAH.

During the course of this doctoral project, the recommended cut-off value of invasive mPAP for diagnosis of PH decreased from 25 mmHg to 20 mmHg. In Study II, an mPAP of 25 mmHg or more indicated PH. In light of the new recommendations, if a vortex duration $\geq$ 10% and TR > 2.7 m/s were considered as indicative of PH, the diagnostic yield would change to 42% vs 24%, for CMR and echocardiography, respectively (p<0.001).

Study III compared 4D flow vortex analysis against invasive measurements with excellent results. Again, not all types of PH were present in similar numbers in this patient cohort and there was a time difference between exam dates. Although one observed a very good correlation between CMR and invasive measurements, the highest mPAP measured invasively was 59 mmHg, which is far from some of the extreme pressures observed in severe cases of PH.

Future studies using the 4D flow analysis method for estimation of PA pressure could also include estimation of mPCWP and PVR, for a comprehensive evaluation of pulmonary hemodynamics. If these methods were proven to accurately estimate these parameters, a comprehensive method for diagnosis of PH (including hemodynamic classification) could one day be part of the routine CMR exam.

Study IV contributed to solving a known problem in CMR flow measurement by introducing a sequence that can accurately measure flow with very high temporal resolution. Interestingly, a systemic underestimation of transmitral velocities persisted (specifically peak E-velocity), while myocardial tissue velocities retained good correlation with Doppler TTE. One may hypothesize that this underestimation is not due an insufficient temporal resolution, but rather to issues with image slice positioning, which tended to be placed too apically. A solution to this problem could be long-axis in-plane acquisition, similarly to the measurements by echocardiography. However, there are significant technical challenges to overcome by this approach. Further development of SWIG could also include a spatial frequency-dependent temporal filter, to further decrease the temporal footprint by limiting the number of k-space spokes that contribute towards the central part of the image.

Lastly, Study V used a combination of the techniques explored in the previous studies and therefore shares some of the limitations already described. Since the patient cohort consisted of a clinical consecutive population, most subjects were diagnosed with acute myocardial ischemia or ischemic heart disease, which likely led to the overrepresentation of Grade I DD. In future studies, it would be beneficial to include other conditions in higher numbers (e.g. amyloidosis, cardiomyopathy, other infiltrative diseases) and to compare CMR with invasive measures of PCWP or LV end-diastolic pressures.

8 SUMMARY AND CONCLUSIONS

"DEATH: Do you never stop questioning?

ANTONIUS BLOCK: No. I never stop."

in The Seventh Seal (*Det sjunde inseglet*, 1957), Ingmar Bergman

Based on the data from all five studies, the main conclusion is that CMR has the potential to become a valid alternative for diagnosis and treatment monitoring in both PH and diastolic dysfunction. Indeed, CMR-based methods were shown to be useful in the evaluation of flow variables of possible diagnostic value (PVDR), and showed very good diagnostic performance in the estimation of mPAP and diagnosis of PH, as well as measurement of diastolic parameters used in the diagnosis of diastolic dysfunction.

The study-specific conclusions are the following:

- **Study I:** In the lateral position, the distribution of pulmonary blood flow shifts to the dependent lung. Furthermore, the non-dependent lung hosts a considerable PVDR, possibly related with left atrial pressure.
- **Study II:** Estimated mPAP from CMR has good quantitative and moderate categorical agreement with TRPG from echocardiography. CMR has higher diagnostic yield than echocardiography for detecting elevated PA pressure.
- **Study III:** Estimated mPAP from CMR has very good agreement with invasively measured mPAP from RHC, and better sensitivity and accuracy than echocardiography.
- **Study IV:** The novel SWIG sequence shows improved temporal resolution compared with other methods, and can measure transmitral and myocardial tissue velocities with low-to-moderate bias compared with echocardiography.
- **Study V:** A comprehensive CMR method for diagnosis and grading of diastolic dysfunction shows very good categorical agreement compared with echocardiography.

9 ACKNOWLEDGEMENTS

"O my soul, now have I given you all, (…) That I bade you sing, say now, say: which of us now owes thanks? Better still, however: sing to me, O my soul! And let me thank you!"

in Thus Spoke Zarathustra (1885), Friedrich Nietzsche

When I was 6 or 7 years old and was asked "What do you want to be when you grow up?", my answer was promptly "A scientist!". I am therefore glad that I decided to pursue a PhD in cardiac imaging at Karolinska Institutet, granting me, as Martin Ugander would say, a researcher's driving license. None of this would be possible without the involvement, hard work, and help of the people whom I thank in this section.

I thank **Martin Ugander**, my main supervisor, for giving me the opportunity of moving to and working on one of the epicenters of medical research in Europe. You provided guidance and inspiration at all times, working closely with me to guarantee that things got well done, but providing enough freedom so that I would find my own way. I hope I can continue to follow the next steps in the Ugander's Algorithm of the Meaning of Life.

Björn Wieslander, my co-supervisor, you were a fellow soldier in the trenchlines, ready at any time to teach how to scan patients, how to look at images and how to think about results. You were a main source of interesting discussions, motivation and stability, especially when the going got tough (and the tough got going). I am convinced ($p<<0.05$) that all this work would have been much more difficult and boring without you. **Andreas Sigfridsson**, also my co-supervisor, thank you for your patience and pedagogic talent in that elusive field that is MR-physics and technology. Your answers and advice, both as MR-physicist and research group leader, were invaluable to me. **John Pernow**, my PhD mentor, thank you for all the sessions we had and interesting conversations, about everything from Cardiology to life and wine.

Alexander Fyrdahl, thank you for being yet another fellow soldier in the trenches, and a technical officer at that. Not only did several of these studies include your direct input and collaboration, but also your ingenuity in fixing things or finding new ways to do them. It was an honor to serve by your side, sir.

I thank all **co-authors** of the studies included in this thesis. Special thanks go to **Michael Melin**, **Patrik Sundblad**, and **Viktoria Skott**, for the amazing cooperation in the METAPHOR project, and **Gert** and **Ursula Reiter**, for coaching me in the mysteries of the PH vortex. I thank **Kenneth Caidahl** for all his help and company during late night research sessions at the HQ.

10 META

When one works in research for a certain period of time, new habits and ways of thinking begin to appear. In particular, I documented semi-rigorously some parameters related to meta-research, the study of science itself at the most basic level. These data pertain to the 44-month period between August 2016 and March 2020:

- I consumed 3.7±0.9 cups of coffee per workday. In January of every year, coffee consumption increased significantly to 4.1±1.0 cups per day. My consumption was slightly greater than the average coffee consumption in Sweden of 3.2 cups per day.
- I ate a total of 204 *skorpor* (cardamom toasties). Yum!
- During the fall semester of 2019, my colleagues and I played 36 ping-pong matches. I won 2 of them ☺
- I sent out approximately 812 work-related emails and received 3122.
- I walked ca. 96 Swedish miles, or exactly 969 km, from my home to work, and back. That's a bit more than the distance between Malmö and Sundsvall.
- I flew a total of 2435 Swedish miles, or approximately 24,356 km, to various conferences and scientific events. That's almost twice the distance between Lisbon and Vladivostok.
- I wrote approximately 40,000 words, counting only the thesis and the five manuscripts. That's the size of a small novel.
- According to Todoist, my producitivity app, the most productive month every year was September, with 45 tasks completed on average, contrasting with an average of 30 tasks year-round.
- I analyzed approximately 562 image stacks, across 210 patients or healthy volunteers. I didn't track time, but if we assume that it takes 1 hour per patient to analyze and register all image data, that's an approximate total of 210 hours of data analysis (without counting training, repeat analyses, inter-observer variability, and failed analyses).

11 REFERENCES

[1]   R. J. Oudiz, "Classification of Pulmonary Hypertension," *Cardiol. Clin.*, vol. 34, no. 3, pp. 359–361, Aug. 2016.

[2]   M. A. Gatzoulis *et al.*, "Updated Clinical Classification of Pulmonary Hypertension," *J. Am. Coll. Cardiol.*, vol. 62, no. 25, pp. D34–D41, 2013.

[3]   D. T. Wijeratne *et al.*, "Increasing Incidence and Prevalence of World Health Organization Groups 1 to 4 Pulmonary Hypertension: A Population-Based Cohort Study in Ontario, Canada.," *Circ. Cardiovasc. Qual. Outcomes*, vol. 11, no. 2, p. e003973, Feb. 2018.

[4]   E. M. Moreira *et al.*, "Prevalence of pulmonary hypertension in the general population: The Rotterdam study," *PLoS One*, vol. 10, no. 6, Jun. 2015.

[5]   S. C. Mathai and V. V. McLaughlin, "Beast of Pulmonary Arterial Hypertension Burden," *JAMA Cardiol.*, vol. 1, no. 9, p. 1030, Dec. 2016.

[6]   N. Hambly, F. Alawfi, and S. Mehta, "Pulmonary hypertension: diagnostic approach and optimal management.," *CMAJ*, vol. 188, no. 11, pp. 804–812, Aug. 2016.

[7]   N. Galiè *et al.*, "2015 ESC/ERS Guidelines for the diagnosis and treatment of pulmonary hypertension," *Eur. Heart J.*, vol. 37, no. 1, 2015.

[8]   F. Parent *et al.*, "A Hemodynamic Study of Pulmonary Hypertension in Sickle Cell Disease," *N. Engl. J. Med.*, vol. 365, no. 1, pp. 44–53, Jul. 2011.

[9]   J. E. Hall, *Guyton and Hall Textbook of Medical Physiology*, 13th ed. Elsevier, 2016.

[10]   M. M. Hoeper *et al.*, "Definitions and Diagnosis of Pulmonary Hypertension," *J. Am. Coll. Cardiol.*, vol. 62, no. 25, pp. D42–D50, 2013.

[11]   N. Saouti, N. Westerhof, P. E. Postmus, and A. Vonk-Noordegraaf, "The arterial load in pulmonary hypertension.," *Eur. Respir. Rev.*, vol. 19, no. 117, pp. 197–203, Sep. 2010.

[12]   S. Mahapatra, R. A. Nishimura, P. Sorajja, S. Cha, and M. D. McGoon, "Relationship of pulmonary arterial capacitance and mortality in idiopathic pulmonary arterial hypertension," *J. Am. Coll. Cardiol.*, vol. 47, no. 4, pp. 799–803, Feb. 2006.

[13]   G. R. Stevens, A. Garcia-Alvarez, S. Sahni, M. J. Garcia, V. Fuster, and J. Sanz, "RV dysfunction in pulmonary hypertension is independently related to pulmonary artery stiffness," *JACC Cardiovasc. Imaging*, vol. 5, no. 4, pp. 378–387, Apr. 2012.

[14]   T. Thenappan, K. W. Prins, M. R. Pritzker, J. Scandurra, K. Volmers, and E. K. Weir, "The Critical Role of Pulmonary Arterial Compliance in Pulmonary Hypertension.," *Ann. Am. Thorac. Soc.*, vol. 13, no. 2, pp. 276–84, Feb. 2016.

[15]   J. W. Lankhaar *et al.*, "Pulmonary vascular resistance and compliance stay inversely related during treatment of pulmonary hypertension," *Eur. Heart J.*, vol. 29, no. 13, pp. 1688–1695, Jul. 2008.

[16]   N. Stergiopulos, J. J. Meister, and N. Westerhof, "Evaluation of methods for estimation of total arterial compliance," *Am. J. Physiol. - Hear. Circ. Physiol.*, vol. 268, no. 4 37-4, 1995.

[17]   G. F. Mitchell, "Arterial stiffness and wave reflection: Biomarkers of cardiovascular risk," *Artery Research*, vol. 3, no. 2. pp. 56–64, Jun-2009.

[18]   V. Castelain, P. Hervé, Y. Lecarpentier, P. Duroux, G. Simonneau, and D. Chemla, "Pulmonary artery pulse pressure and wave reflection in chronic pulmonary thromboembolism and primary pulmonary hypertension," *J. Am. Coll. Cardiol.*, vol. 37, no. 4, pp. 1085–1092, Mar. 2001.

[19]   N. Lan, B. Massam, S. Kulkarni, and C. Lang, "Pulmonary Arterial Hypertension: Pathophysiology and Treatment," *Diseases*, vol. 6, no. 2, p. 38, May 2018.

[20]   W. Tan, K. Madhavan, K. S. Hunter, D. Park, and K. R. Stenmark, "Vascular stiffening in pulmonary hypertension: Cause or consequence? (2013 Grover conference series)," *Pulmonary Circulation*, vol. 4, no. 4. University of Chicago Press, pp. 560–580, 01-Dec-2014.

[21]   R. M. Tuder *et al.*, "Relevant issues in the pathology and pathobiology of pulmonary hypertension," in *Journal of the American College of Cardiology*, 2013, vol. 62, no. 25 SUPPL.

[22]   A. Charalampopoulos *et al.*, "Pathophysiology and diagnosis of pulmonary hypertension due to left heart disease," *Frontiers in Medicine*, vol. 5, no. JUN. Frontiers Media S.A., 01-Jun-2018.

[23]   J. Vendrik, E. S. Farag, N. H. L. C. de Hoon, J. Kluin, and J. Baan, "Presence of aortic root vortex formation after TAVI with CENTERA confirmed using 4D-flow magnetic resonance imaging," *Int. J. Cardiovasc. Imaging*, vol. 34, no. 12, pp. 1947–1948, Dec. 2018.

[24]   P. S. Pagel, B. T. Boettcher, D. J. De Vry, J. K. Freed, and Z. Iqbal, "Moderate Aortic Valvular Insufficiency Invalidates Vortex Formation Time as an Index of Left Ventricular Filling Efficiency in Patients With Severe Degenerative Calcific Aortic Stenosis Undergoing Aortic Valve Replacement," *J. Cardiothorac. Vasc. Anesth.*, vol. 30, no. 5, pp. 1260–1265, Oct. 2016.

[25]   G. Reiter *et al.*, "Magnetic resonance-derived 3-dimensional blood flow patterns in the main pulmonary artery as a marker of pulmonary hypertension and a measure of elevated mean pulmonary arterial pressure.," *Circ. Cardiovasc. Imaging*, vol. 1, no. 1, pp. 23–30, 2008.

[26]   G. Reiter, U. Reiter, G. Kovacs, H. Olschewski, and M. Fuchsjäger, "Blood flow vortices along the main pulmonary artery measured with MR imaging for diagnosis of pulmonary hypertension.," *Radiology*, vol. 275, no. 1, pp. 71–9, 2015.

[27]   M. Tahara *et al.*, "Hemodynamic determinants of pulmonary valve motion during systole in experimental pulmonary hypertension.," *Circulation*, vol. 64, no. 6, pp. 1249–55, Dec. 1981.

[28]   A. Kheradvar and G. Pedrizzeti, *Vortex Formation in the Cardiovascular System*. Springer, 2012.

[29]   M. Ugander *et al.*, "Pulmonary Blood Volume Variation Decreases after Myocardial Infarction in Pigs: A Quantitative and Noninvasive MR Imaging Measure of Heart Failure 1," *Radiology*, vol. 256.

[30]   M. Ugander, E. Jense, and H. Arheden, "Pulmonary intravascular blood volume

changes through the cardiac cycle in healthy volunteers studied by cardiovascular magnetic resonance measurements of arterial and venous flow.," *J. Cardiovasc. Magn. Reson.*, vol. 11, no. 1, p. 42, Oct. 2009.

[31] H. C. Champion, E. D. Michelakis, and P. M. Hassoun, "Comprehensive invasive and noninvasive approach to the right ventricle-pulmonary circulation unit state of the art and clinical and research implications," *Circulation*, vol. 120, no. 11. pp. 992–1007, 2009.

[32] N. Galiè *et al.*, "2015 ESC/ERS Guidelines for the diagnosis and treatment of pulmonary hypertension," *Eur. Heart J.*, vol. 37, no. 1, pp. 67–119, Jan. 2016.

[33] G. Habib and A. Torbicki, "The role of echocardiography in the diagnosis and management of patients with pulmonary hypertension," *Eur. Respir. Rev.*, vol. 19, no. 118, pp. 288–299, Dec. 2010.

[34] J. F. Aduen *et al.*, "Accuracy and precision of three echocardiographic methods for estimating mean pulmonary artery pressure.," *Chest*, vol. 139, no. 2, pp. 347–352, Feb. 2011.

[35] C. Magnino *et al.*, "Inaccuracy of Right Atrial Pressure Estimates Through Inferior Vena Cava Indices," *Am. J. Cardiol.*, vol. 120, no. 9, pp. 1667–1673, Nov. 2017.

[36] F. Ferrara *et al.*, "Echocardiography in Pulmonary Arterial Hypertension," *Curr. Cardiol. Rep.*, vol. 21, no. 4, p. 22, Apr. 2019.

[37] N. Galiè *et al.*, "2015 ESC/ERS Guidelines for the diagnosis and treatment of pulmonary hypertension," *Eur. Heart J.*, vol. 37, no. 1, pp. 67–119, 2015.

[38] S. M. Arcasoy *et al.*, "Echocardiographic assessment of pulmonary hypertension in patients with advanced lung disease," *Am. J. Respir. Crit. Care Med.*, vol. 167, no. 5, pp. 735–740, Mar. 2003.

[39] H. W. Farber, A. J. Foreman, D. P. Miller, and M. D. McGoon, "REVEAL Registry: Correlation of Right Heart Catheterization and Echocardiography in Patients With Pulmonary Arterial Hypertension," *Congest. Hear. Fail.*, vol. 17, no. 2, pp. 56–63, Mar. 2011.

[40] T. Pawade, B. Holloway, W. Bradlow, and R. P. Steeds, "Noninvasive imaging for the diagnosis and prognosis of pulmonary hypertension," *Expert Rev. Cardiovasc. Ther.*, vol. 12, no. 1, pp. 71–86, Jan. 2014.

[41] G. Strange *et al.*, "Threshold of Pulmonary Hypertension Associated With Increased Mortality," *J. Am. Coll. Cardiol.*, vol. 73, no. 21, pp. 2660–2672, Jun. 2019.

[42] F. Grothues, J. C. Moon, N. G. Bellenger, G. S. Smith, H. U. Klein, and D. J. Pennell, "Interstudy reproducibility of right ventricular volumes, function, and mass with cardiovascular magnetic resonance," *Am. Heart J.*, vol. 147, no. 2, pp. 218–223, 2004.

[43] S. A. Van Wolferen *et al.*, "Prognostic value of right ventricular mass, volume, and function in idiopathic pulmonary arterial hypertension," *Eur. Heart J.*, vol. 28, no. 10, pp. 1250–1257, May 2007.

[44] K. G. Blyth *et al.*, "Contrast enhanced-cardiovascular magnetic resonance imaging in patients with pulmonary hypertension," *Eur. Heart J.*, vol. 26, no. 19, pp. 1993–1999, Oct. 2005.

[45] J. Sanz *et al.*, "Pulmonary arterial hypertension: Noninvasive detection with phase-contrast MR imaging," *Radiology*, vol. 243, no. 1, pp. 70–79, Apr. 2007.

[46] A. J. Swift *et al.*, "Diagnostic accuracy of cardiovascular magnetic resonance imaging of right ventricular morphology and function in the assessment of suspected pulmonary hypertension results from the ASPIRE registry," *J. Cardiovasc. Magn. Reson.*, vol. 14, no. 1, p. 40, Dec. 2012.

[47] F. Helderman, G.-J. Mauritz, K. E. Andringa, A. Vonk-Noordegraaf, and J. T. Marcus, "Early onset of retrograde flow in the main pulmonary artery is a characteristic of pulmonary arterial hypertension," *J. Magn. Reson. Imaging*, vol. 33, no. 6, pp. 1362–1368, Jun. 2011.

[48] E. Laffon *et al.*, "A computed method for noninvasive MRI assessment of pulmonary arterial hypertension," *J. Appl. Physiol.*, vol. 96, no. 2, pp. 463–468, Feb. 2004.

[49] K. F. Kreitner *et al.*, "Noninvasive assessment of pulmonary hemodynamics in patients with chronic thromboembolic pulmonary hypertension by high temporal resolution phase-contrast MRI: Correlation with simultaneous invasive pressure recordings," *Circ. Cardiovasc. Imaging*, vol. 6, no. 5, pp. 722–729, Sep. 2013.

[50] V. Kumar, *Robbins & Cotran Pathologic Basis of Disease*. Elsevier, 2017.

[51] I. Lakhani, K. S. K. Leung, G. Tse, and A. P. W. Lee, "Novel mechanisms in heart failure with preserved, midrange, and reduced ejection fraction," *Frontiers in Physiology*, vol. 10, no. JUL. Frontiers Media S.A., 2019.

[52] A. Abbate *et al.*, "Heart failure with preserved ejection fraction: Refocusing on diastole," *Int. J. Cardiol.*, vol. 179, pp. 430–440, Jan. 2015.

[53] E.-M. Jeong and S. C. Dudley Jr, "Diastolic Dysfunction," *Circ. J.*, vol. 79, no. 3, pp. 470–477, 2015.

[54] G. W. K. Yip *et al.*, "The Hong Kong diastolic heart failure study: A randomised controlled trial of diuretics, irbesartan and ramipril on quality of life, exercise capacity, left ventricular global and regional function in heart failure with a normal ejection fraction," *Heart*, vol. 94, no. 5, pp. 573–580, May 2008.

[55] M. M. Redfield, S. J. Jacobsen, J. C. Burnett, Jr, D. W. Mahoney, K. R. Bailey, and R. J. Rodeheffer, "Burden of Systolic and Diastolic Ventricular Dysfunction in the Community," *JAMA*, vol. 289, no. 2, p. 194, Jan. 2003.

[56] Z. B. Popović, K. Sato, and M. Y. Desai, "Is universal grading of diastolic function by echocardiography feasible?," *Cardiovascular Diagnosis and Therapy*, vol. 8, no. 1. AME Publishing Company, pp. 18–28, 01-Feb-2018.

[57] T. T. Phan and M. Frenneaux, "The pathophysiology of diastolic heart failure," *F1000 Biology Reports*, vol. 2, no. 1. 24-Feb-2010.

[58] O. S. Andersen *et al.*, "Estimating Left Ventricular Filling Pressure by Echocardiography," *J. Am. Coll. Cardiol.*, vol. 69, no. 15, pp. 1937–1948, Apr. 2017.

[59] A. M. Shah *et al.*, "Cardiac structure and function in heart failure with preserved ejection fraction: Baseline findings from the echocardiographic study of the treatment of preserved cardiac function heart failure with an aldosterone antagonist trial," *Circ.*

Hear. Fail., vol. 7, no. 1, pp. 104–115, 2014.

[60] S. E. Litwin and M. R. Zile, "Should We Test for Diastolic Dysfunction? How and How Often?," *JACC Cardiovasc. Imaging*, Jun. 2019.

[61] A. Borbély *et al.*, "Cardiomyocyte stiffness in diastolic heart failure," *Circulation*, vol. 111, no. 6, pp. 774–781, Feb. 2005.

[62] A. L. Reed *et al.*, "Diastolic dysfunction is associated with cardiac fibrosis in the senescence-accelerated mouse," *Am. J. Physiol. - Hear. Circ. Physiol.*, vol. 301, no. 3, Sep. 2011.

[63] E.-M. Jeong, S. C. Dudley, and Jr., "New diagnostic and therapeutic possibilities for diastolic heart failure.," *R. I. Med. J. (2013)*, vol. 97, no. 2, pp. 35–7, Feb. 2014.

[64] M. R. Zile *et al.*, "Prevalence and significance of alterations in cardiac structure and function in patients with heart failure and a preserved ejection fraction," *Circulation*, vol. 124, no. 23, pp. 2491–2501, Dec. 2011.

[65] M. Afshar, F. Collado, and R. Doukky, "Pulmonary Hypertension in Elderly Patients with Diastolic Dysfunction and Preserved Ejection Fraction," *Open Cardiovasc. Med. J.*, vol. 6, no. 1, pp. 1–8, Jan. 2012.

[66] Y. Neuman, A. Kotliroff, T. Bental, R. J. Siegel, D. David, and M. Lishner, "Pulmonary artery pressure and diastolic dysfunction in normal left ventricular systolic function," *Int. J. Cardiol.*, vol. 127, no. 2, pp. 174–178, Jul. 2008.

[67] M. Garbi *et al.*, "Appropriateness criteria for cardiovascular imaging use in heart failure: report of literature review On behalf of the EACVI Imaging Task Force."

[68] P. Ponikowski *et al.*, "2016 ESC Guidelines for the diagnosis and treatment of acute and chronic heart failure," *European Heart Journal*, vol. 37, no. 27. Johann Bauersachs, pp. 2129-2200m, 2016.

[69] H. S. Norman *et al.*, "Decreased Cardiac Functional Reserve in Heart Failure With Preserved Systolic Function," *J. Card. Fail.*, vol. 17, no. 4, pp. 301–308, Apr. 2011.

[70] J. J. M. Westenberg, "CMR for Assessment of Diastolic Function.," *Curr. Cardiovasc. Imaging Rep.*, vol. 4, no. 2, pp. 149–158, Apr. 2011.

[71] S. F. Nagueh *et al.*, "Recommendations for the Evaluation of Left Ventricular Diastolic Function by Echocardiography: An Update from the American Society of Echocardiography and the European Association of Cardiovascular Imaging," *J. Am. Soc. Echocardiogr.*, vol. 29, no. 4, pp. 277–314, Apr. 2016.

[72] W. Zhang and S. J. Kovács, "The Age Dependence of Left Ventricular Filling Efficiency," *Ultrasound Med. Biol.*, vol. 35, no. 7, pp. 1076–1085, Jul. 2009.

[73] M. Wang *et al.*, "Peak early diastolic mitral annulus velocity by tissue Doppler imaging adds independent and incremental prognostic value.," *J. Am. Coll. Cardiol.*, vol. 41, no. 5, pp. 820–6, Mar. 2003.

[74] D. W. Sohn *et al.*, "Mitral annulus velocity in the evaluation of left ventricular diastolic function in atrial fibrillation.," *J. Am. Soc. Echocardiogr.*, vol. 12, no. 11, pp. 927–31, Nov. 1999.

[75] M. Zareian *et al.*, "Left atrial structure and functional quantitation using

cardiovascular magnetic resonance and multimodality tissue tracking: validation and reproducibility assessment," *J. Cardiovasc. Magn. Reson.*, vol. 17, no. 1, p. 52, Dec. 2015.

[76] P. S. Douglas, "The left atrium: A biomarker of chronic diastolic dysfunction and cardiovascular disease risk," *Journal of the American College of Cardiology*, vol. 42, no. 7. Elsevier Inc., pp. 1206–1207, 01-Oct-2003.

[77] O. S. Andersen *et al.*, "Estimating Left Ventricular Filling Pressure by Echocardiography," *J. Am. Coll. Cardiol.*, vol. 69, no. 15, pp. 1937–1948, Apr. 2017.

[78] P. Lancellotti *et al.*, "Echo-Doppler estimation of left ventricular filling pressure: results of the multicentre EACVI Euro-Filling study," *Eur. Hear. J. - Cardiovasc. Imaging*, vol. 18, no. 9, pp. 961–968, Sep. 2017.

[79] V. K. Rathi *et al.*, "Routine evaluation of left ventricular diastolic function by cardiovascular magnetic resonance: A practical approach," *J. Cardiovasc. Magn. Reson.*, vol. 10, no. 1, p. 36, Dec. 2008.

[80] J. Caudron, J. Fares, F. Bauer, and J.-N. Dacher, "Evaluation of Left Ventricular Diastolic Function with Cardiac MR Imaging," *RadioGraphics*, vol. 31, no. 1, pp. 239–259, Jan. 2011.

[81] T. Edvardsen *et al.*, "Regional diastolic dysfunction in individuals with left ventricular hypertrophy measured by tagged magnetic resonance imaging—The Multi-Ethnic Study of Atherosclerosis (MESA)," *Am. Heart J.*, vol. 151, no. 1, pp. 109–114, Jan. 2006.

[82] T. Elgeti *et al.*, "Cardiac MR Elastography: Comparison with left ventricular pressure measurement," *J. Cardiovasc. Magn. Reson.*, vol. 11, no. 1, 2009.

[83] D. G. Nishimura, *Principles of Magnetic Resonance Imaging*, 1.2. Self-published, 2016.

[84] O. Bieri and K. Scheffler, "Fundamentals of balanced steady state free precession MRI," *J. Magn. Reson. Imaging*, vol. 38, no. 1, pp. 2–11, 2013.

[85] M. Salerno *et al.*, "Recent Advances in Cardiovascular Magnetic Resonance," *Circ. Cardiovasc. Imaging*, vol. 10, no. 6, Jun. 2017.

[86] C. M. Kramer, J. Barkhausen, C. Bucciarelli-Ducci, S. D. Flamm, R. J. Kim, and E. Nagel, "Standardized cardiovascular magnetic resonance imaging (CMR) protocols: 2020 update.," *J. Cardiovasc. Magn. Reson.*, vol. 22, no. 1, p. 17, Feb. 2020.

[87] S. Valbuena-López, R. Hinojar, and V. O. Puntmann, "Cardiovascular Magnetic Resonance in Cardiology Practice: A Concise Guide to Image Acquisition and Clinical Interpretation," *Rev. Española Cardiol. (English Ed.*, vol. 69, no. 2, pp. 202–210, Feb. 2016.

[88] U. Reiter, G. Reiter, and M. F. Ager, "MR phase-contrast imaging in pulmonary hypertension," *Br J Radiol*, vol. 89, 2016.

[89] A. Fyrdahl, J. G. Ramos, M. J. Eriksson, K. Caidahl, M. Ugander, and A. Sigfridsson, "Sector-wise golden-angle phase contrast with high temporal resolution for evaluation of left ventricular diastolic dysfunction," *Magn. Reson. Med.*, vol. 83, no. 4, pp. 1310–

1321, Apr. 2020.

[90] E. Heiberg, J. Sjögren, M. Ugander, M. Carlsson, H. Engblom, and H. Arheden, "Design and validation of Segment--freely available software for cardiovascular image analysis.," *BMC Med. Imaging*, vol. 10, no. 1, p. 1, Jan. 2010.

[91] B. Rosner, *Fundamentals of Biostatistics*, 7th Editio. Wadsworth CENAGE Learning, 2010.

[92] R. J. Woodman, "Bland-Altman beyond the basics: Creating confidence with badly behaved data," *Clinical and Experimental Pharmacology and Physiology*, vol. 37, no. 2. pp. 141–142, Feb-2010.

[93] E. R. DeLong, D. M. DeLong, and D. L. Clarke-Pearson, "Comparing the Areas under Two or More Correlated Receiver Operating Characteristic Curves: A Nonparametric Approach," *Biometrics*, vol. 44, no. 3, p. 837, Sep. 1988.

[94] P. F. Watson and A. Petrie, "Method agreement analysis: A review of correct methodology," *Theriogenology*, vol. 73, no. 9. Elsevier, pp. 1167–1179, 01-Jun-2010.

[95] J. Cohen, "Weighted kappa: Nominal scale agreement provision for scaled disagreement or partial credit," *Psychol. Bull.*, vol. 70, no. 4, pp. 213–220, Oct. 1968.

[96] "World Medical Association declaration of Helsinki: Ethical principles for medical research involving human subjects," *JAMA - Journal of the American Medical Association*, vol. 310, no. 20. pp. 2191–2194, 2013.

[97] M. Whitlock, A. Garg, J. Gelow, T. Jacobson, and C. Broberg, "Comparison of Left and Right Atrial Volume by Echocardiography Versus Cardiac Magnetic Resonance Imaging Using the Area-Length Method," *Am. J. Cardiol.*, vol. 106, no. 9, pp. 1345–1350, Nov. 2010.